



Universiteit
Leiden
The Netherlands

Copper ionophore elesclomol selectively targets GNAQ/11-mutant uveal melanoma

Li, Y.Y.; Yang, J.; Zhang, Q.Q.; Xu, S.Q.; Sun, W.; Ge, S.F.; ... ; Fan, X.Q.

Citation

Li, Y. Y., Yang, J., Zhang, Q. Q., Xu, S. Q., Sun, W., Ge, S. F., ... Fan, X. Q. (2022). Copper ionophore elesclomol selectively targets GNAQ/11-mutant uveal melanoma. *Oncogene*, 41(27), 3539-3553. doi:10.1038/s41388-022-02364-0

Version: Publisher's Version

License: [Leiden University Non-exclusive license](#)

Downloaded from: <https://hdl.handle.net/1887/3485612>

Note: To cite this publication please use the final published version (if applicable).

ARTICLE



Copper ionophore elesclomol selectively targets *GNAQ/11*-mutant uveal melanoma

Yongyun Li^{1,2,6}, Jie Yang^{1,2,6}, Qianqian Zhang³, Shiqiong Xu^{1,2}, Wei Sun³, Shengfang Ge^{1,2}, Xiaowei Xu⁴, Martine J. Jager⁵, Renbing Jia^{1,2,7} , Jianming Zhang^{3,7}  and Xianqun Fan^{1,2,7} 

© The Author(s), under exclusive licence to Springer Nature Limited 2022

Unlike cutaneous melanoma, uveal melanoma (UM) is characterized by mutations in *GNAQ* and *GNA11* and remains a fatal disease because there is essentially no effective targeted therapy or immunotherapy available. We report the discovery of the copper ionophore elesclomol as a *GNAQ/11*-specific UM inhibitor. Elesclomol was identified in a differential cytotoxicity screen of an in-house tool compound library, and its *in vivo* pharmacological efficacy was further confirmed in zebrafish and mouse UM models. Mechanistically, elesclomol transports copper to mitochondria and produces a large amount of reactive oxygen species (ROS) as Cu(II) is reduced to Cu(I) in *GNAQ/11*-mutant UM cells, which selectively activates LATS1 kinase in the Hippo signaling pathway and consequently promotes YAP phosphorylation and inhibits its nuclear accumulation. The inactivation of YAP downregulates the expression of *SNAI2*, which in turn suppresses the migration of UM cells. These findings were cross validated by our clinical observation that YAP activation was found specifically in UM samples with a *GNAQ/11* mutation. Furthermore, addition of binimetinib, a MEK inhibitor, to elesclomol increased its synthetic lethality to *GNAQ/11*-mutant UM cells, thereby overriding drug resistance. This effect was confirmed in an orthotopic xenograft model and in a patient-derived xenograft model of UM. These studies reveal a novel mechanistic basis for repurposing elesclomol by showing that copper homeostasis is a *GNAQ/11*-specific vulnerability in UM. Elesclomol may provide a new therapeutic path for selectively targeting malignant *GNAQ/11*-mutant UM.

Oncogene (2022) 41:3539–3553; <https://doi.org/10.1038/s41388-022-02364-0>

INTRODUCTION

Uveal melanoma (UM) is the most common primary intraocular malignancy in adults, of whom approximately half will develop metastases, predominantly in the liver [1, 2]. Once metastases occur, the median progression-free survival (PFS) and overall survival (OS) are only 3.3 and 10.2 months, respectively [3]. This extremely low survival rate is attributed not only to the malignant nature of UM but also to the lack of effective clinical treatments. More than 80% of patients with UM harbor a mutation in *guanine nucleotide-binding protein G(q) subunit alpha (GNAQ)* or *guanine nucleotide-binding protein G(11) subunit alpha (GNA11)* [4–6]. $G\alpha_q$ and $G\alpha_{11}$, encoded by *GNAQ* and *GNA11*, are α subunits of a heterotrimeric G protein, which plays an important role in G protein-coupled receptor (GPCR) signaling. Interestingly, mutations in *GNAQ* or *GNA11* occur in a mutually exclusive manner, in arginine 183 (R183) or glutamine 209 (Q209). R183 and Q209 are located in the switch I and switch II domains of the $G\alpha_{q/11}$ subunits, respectively. These mutations continuously activate G protein by entirely crippling its GTPase activity [7]. Mutant constitutively activated $G\alpha_q$ and $G\alpha_{11}$ drive abnormal proliferative signaling, including the MAPK/MEK/ERK, Trio/Rho/Rac/YAP and PI3K/Akt/mTOR pathways [8–10].

The discovery of agents that directly target mutant $G\alpha_q$ or $G\alpha_{11}$ or their signaling pathways would present a compelling approach to treat UM with a $G\alpha_q$ or $G\alpha_{11}$ mutation. However, thus far, the only $G\alpha_{q/11}$ inhibitors identified are a series of natural products represented by YM-254890 and FR900359 [11]. These two natural products specifically inhibit $G\alpha_{q/11}$ -mediated signal transduction and cellular proliferation in UM cells that carry a *GNAQ/11*^{Q209} mutation [12, 13]. Nevertheless, the complex structure and difficulties in synthesis or production of these natural products have impeded their preclinical development. The drug-like properties of these compounds and their exact pharmacological efficacies *in vivo* need to be further investigated.

Alternatively, targeting $G\alpha_{q/11}$ -mediated signaling pathways has proven to be extremely challenging because *GNAQ* and *GNA11* mutations activate multiple signaling pathways to orchestrate disease progression. For instance, a review of 590 cases from six eligible clinical studies showed that UM is poorly responsive to MEK inhibitors, including selumetinib (median PFS 16 weeks, median OS 11.8 months, 14% partial response (PR), 1-year OS rate 45%) and trametinib (median PFS 1.8 months, overall response rate (ORR)/PR/complete response (CR) 0%) [14]. Distinct from skin cutaneous melanoma (SKCM), where the combination of MEK and

¹Department of Ophthalmology, Ninth People's Hospital, Shanghai Jiao Tong University School of Medicine, Shanghai, China. ²Shanghai Key Laboratory of Orbital Diseases and Ocular Oncology, Shanghai, China. ³National Research Center for Translational Medicine (Shanghai), State Key Laboratory of Medical Genomics, Ruijin Hospital, Shanghai Jiao Tong University School of Medicine, Shanghai, China. ⁴Department of Pathology and Laboratory Medicine, University of Pennsylvania, Philadelphia, PA, USA. ⁵Department of Ophthalmology, Leiden University Medical Center, Leiden, The Netherlands. ⁶These authors contributed equally: Yongyun Li, Jie Yang ⁷These authors jointly supervised this work: Renbing Jia, Jianming Zhang, Xianqun Fan. ✉email: renbingjia@sjtu.edu.cn; jzuc@shsmu.edu.cn; fanxq@sjtu.edu.cn

Received: 18 October 2021 Revised: 18 May 2022 Accepted: 26 May 2022

Published online: 13 June 2022

BRAF inhibitors benefits metastatic patients with *BRAF*^{V600E} or *V600K* mutations [15], *GNAQ/11* mutations activate other cascades, such as PI3K/Akt/mTOR and Trio/Rho/Rac/YAP; thus, blocking the RAF/MEK/ERK pathway alone is not sufficient to achieve a satisfactory therapeutic effect in UM. The combination of selumetinib with the AKT inhibitor MK2206 induced synergistic inhibition of *GNAQ*-mutant UM cells in vitro and in vivo [16]. However, a phase II clinical trial of trametinib combined with the AKT inhibitor GSK795 showed no improvement in either the PFS or the response rate (RR) compared with those in the selumetinib group (NCT01979523) [17]. Therefore, it is urgent to find effective therapies that specifically target *GNAQ/11*-mutant UM, especially for tumors that are resistant to MEK inhibitors. To achieve this goal, we performed a differential cytotoxicity screen in a 384-well format of an in-house tool compound library composed of 3541 known target chemicals.

Here, we report that the copper ionophore elesclomol possesses excellent selectivity against *GNAQ/11*-mutant UM cell lines and maintains its therapeutic efficacy in patient-derived tumor cells in an ex vivo model. Elesclomol forms a complex with Cu(II). Cells are able to effectively transport these copper molecules to mitochondria [18]. Through a redox reaction, copper is reduced to its Cu(I) state, and then, free reactive oxygen species (ROS) are produced through the Fenton reaction [18, 19]. In fact, elesclomol is a clinical stage compound that has previously been used alone or in combination with paclitaxel but failed in relapsed or refractory acute myeloid leukemia [20], ovarian cancer [21], refractory solid tumors [22] and SKCM [23, 24]. We were prompted

to ask three questions about repurposing elesclomol. First, why are *GNAQ/11*-mutant UM cells particularly sensitive to elesclomol? Second, what is the molecular mechanism and clinical relevance of elesclomol-triggered copper-dependent cell death? Third, is our understanding of the *GNAQ/11*-specific mode of action of elesclomol sufficient to repurpose this compound for the treatment of UM?

RESULTS

Elesclomol selectively inhibits *GNAQ/11*-mutant UM cells

To discover *GNAQ/11*-specific compounds, the proliferation ratio of seven UM cell lines was examined by screening a chemical library composed of 3541 known target compounds. Among the seven cell lines, 92.1, OMM2.3, and XMP46 carry a *GNAQ*^{Q209} mutation, OMM1 is *GNA11*^{Q209}-mutant, and Mel285, Mel290, and MUM2B are *GNAQ/11*-wild-type (Fig. 1A). In addition to searching for drugs with immediate clinical application, we intended to use this large set of compounds with drug-like properties as chemical probes to decipher any potential vulnerability of *GNAQ/11*-mutant cells. Elesclomol was on the top of the list of drugs that efficiently kill UM cells, with a \log_2 fold change (compound/DMSO) (\log_2 FC) at -3.064 (Fig. 1B). By further examining the half maximal inhibitory concentration (IC_{50}) and target selection, the preference of 74 candidate compounds for *GNAQ/11*-mutant or *GNAQ/11*-wild-type cells was determined using the index \log_{10} (relative IC_{50} ratio) (Supplementary Table 1, Fig. 1C). Dinaciclib, elesclomol, fimepinostat, and alvocidib stood out for their selectivity and

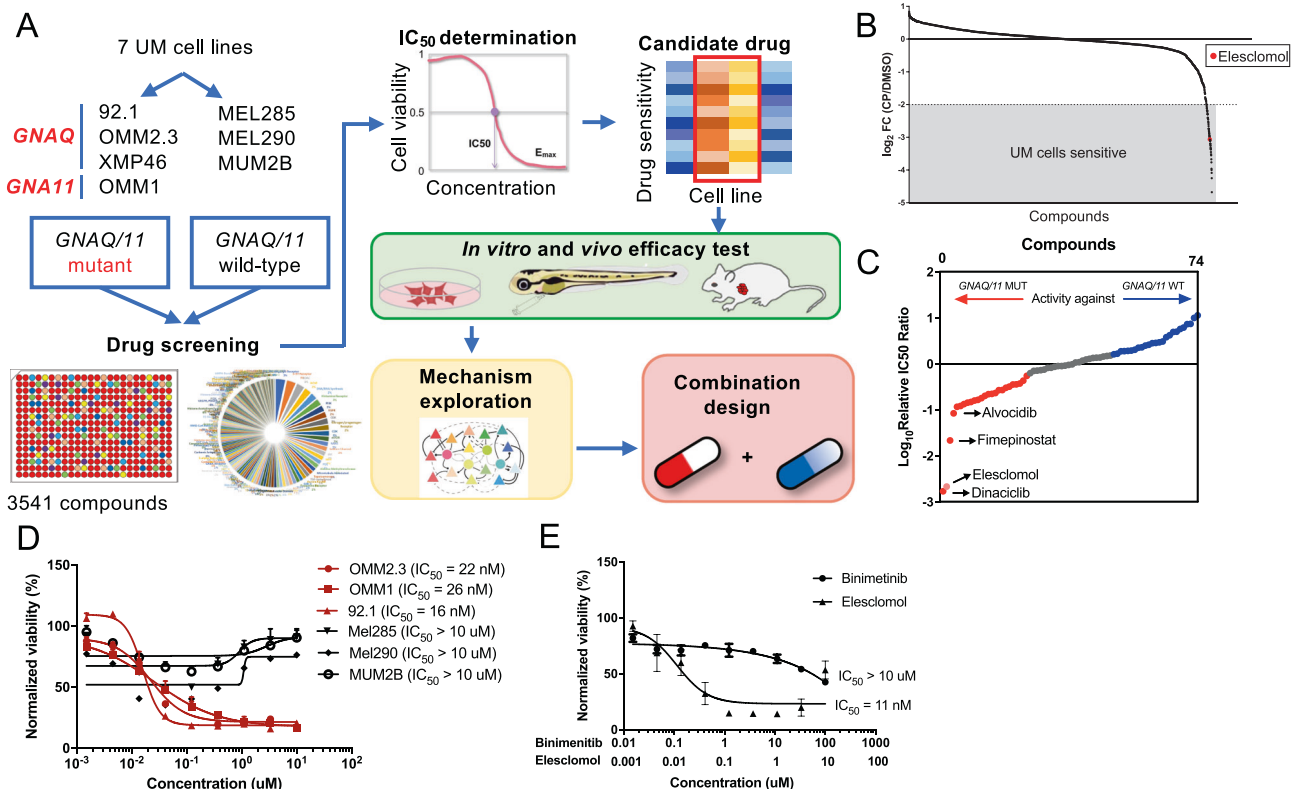


Fig. 1 Discovery of the *GNAQ/11*-specific compound elesclomol. **A** A schematic diagram of drug screening and experimental flow. **B** Overview of the potency of all compounds represented by cell viability. When compounds had a \log_2 FC (compound/DMSO) below -2 , they were defined as UM sensitive. The red dot indicates the position of elesclomol. **C** Relative IC_{50} ratio of 74 hits against *GNAQ/11*-mutant and *GNAQ/11*-wild-type UM cells on the logarithmic (base 10) scale. Red, gray and blue dots represent the strength gradient of the effectiveness of compounds against *GNAQ/11*-mutant cells from strong to weak. The black arrow points to elesclomol. **D** Representative elesclomol dose-response curves in six UM cell lines: *GNAQ/11*-mutant 92.1, OMM2.3, and OMM1 cells and *GNAQ/11*-wild-type Mel285, Mel290, and MUM2B cells. **E** Representative dose-response curve of a primary UM-derived cell line to elesclomol and binimetinib. Error bars represent the mean \pm SEM, $n = 2$ independent experiments for (B), $n = 3$ independent experiments for (D, E).

potency against *GNAQ/11*-mutant UM cells, while protease inhibitors specifically suppressed the growth of *GNAQ/11*-wild-type cells. Dinaciclib and alvocidib are inhibitors of various members of the cyclin-dependent kinase (CDK) family [25, 26]. Fimepinostat is a dual PI3K and histone deacetylase (HDAC) inhibitor [27]. As we looked for specificity, elesclomol showed low IC_{50} values against the *GNAQ/11*-mutant cell lines 92.1 (16 nM), OMM2.3 (22 nM), and OMM1 (26 nM). However, the *GNAQ/11*-wild-type cell lines Mel285, Mel290, and MUM2B were robustly resistant to elesclomol, with IC_{50} values higher than 10 μ M (Fig. 1D).

To confirm the above pharmacological efficacy, elesclomol was evaluated in a culture of patient-derived UM cells with a *GNAQ*^{Q209L} mutation. Elesclomol inhibited the growth of tumor cells with an impressive IC_{50} of 11 nM, while the MEK inhibitor binimetinib was mostly ineffective, with an IC_{50} above 10 μ M (Fig. 1E). These results demonstrate that *GNAQ/11*-mutant UM cells are much more sensitive to elesclomol than *GNAQ/11*-wild-type cells.

***GNAQ/11*-specific cellular events caused by elesclomol**

Elesclomol can effectively transport copper into cells and directly impair mitochondria in several cancer cell lines by increasing the cellular ROS level to an unsustainable level through the reduction reaction of Cu(II) to Cu(I) [18, 19]. We asked whether UM cells with different genetic backgrounds had different capacities to manage cellular ROS. After exposure to 100 nM elesclomol for 3 h, intracellular ROS levels were examined. Compared with the vehicle control, elesclomol significantly increased intracellular ROS levels in *GNAQ/11*-mutant cells ($p < 0.001$) (Fig. 2A, Supplementary Fig. 1A), which is consistent with several previous studies in other cancer types [28]. Cotreatment with 1 mM acetylcysteine (N-acetyl-L-cysteine, NAC, an ROS scavenger) and 2.5 μ M rotenone (a mitochondrial electron transport chain I inhibitor) efficiently blocked the cellular ROS production induced by elesclomol. However, after treatment of *GNAQ/11*-wild-type cells with elesclomol, ROS levels were not significantly higher than after treatment with the vehicle, indicating that wild-type cells balance oxidative stress through another mechanism. We next examined whether elesclomol triggers NRF2 activation, as NRF2 senses cellular oxidative stress and translocates to the nucleus, stimulating the transcription of antioxidant genes that protect cells from ROS cytotoxicity [29]. Following elesclomol treatment at 100 nM for 3 h, NRF2 only showed a tendency toward nuclear localization in *GNAQ/11*-mutant cells ($p < 0.001$) (Fig. 2B, Supplementary Fig. 1B). These results suggest that the *GNAQ/11*-mutant cell lines OMM2.3 and OMM1 are more susceptible to oxidative stress.

To further explore the differential responses of gene transcription and signaling pathways to elesclomol treatment, RNA sequencing (RNA-seq) was performed on *GNAQ/11*-mutant 92.1 cells and *GNAQ/11*-wild-type Mel285 cells, which had been treated with 25 nM elesclomol for 24 h (Supplementary Fig. 1C). In the 92.1 cell line, 186 genes were identified as being differentially expressed, while in the Mel285 cell line, only 8 genes were affected (p value < 0.05 and $FC > 2$) (Fig. 2C). Gene set enrichment analysis (GSEA) revealed that oxidative phosphorylation (OXPHOS) and peroxisome-related gene expression were downregulated, while apoptosis, hypoxia, and TNF α signaling via NF κ B gene expression were upregulated in 92.1 cells ($p < 0.05$ or p adjusted < 0.25) (Fig. 2D, E). Further comparing the genomic expression signatures of 92.1 and Mel285 cells, it was found that the expression levels of genes associated with epithelial–mesenchymal transition (EMT), hypoxia and TNF α signaling via NF κ B were significantly higher in Mel285 cells, while ultraviolet (UV) response-related signaling was downregulated (Supplementary Fig. 1D). These results revealed that *GNAQ/11*-mutant cells were more dependent on OXPHOS pathways and were vulnerable to oxidative stress induced by elesclomol.

To verify that binding with copper is the key mechanism underlying the killing effect of elesclomol on UM cells, an ES analog lacking copper binding capacity was designed (Fig. 2F,

Supplementary Fig. 2A). The IC_{50} values of the analog against 92.1 and OMM2.3 cells were much higher than those of elesclomol (Fig. 2G).

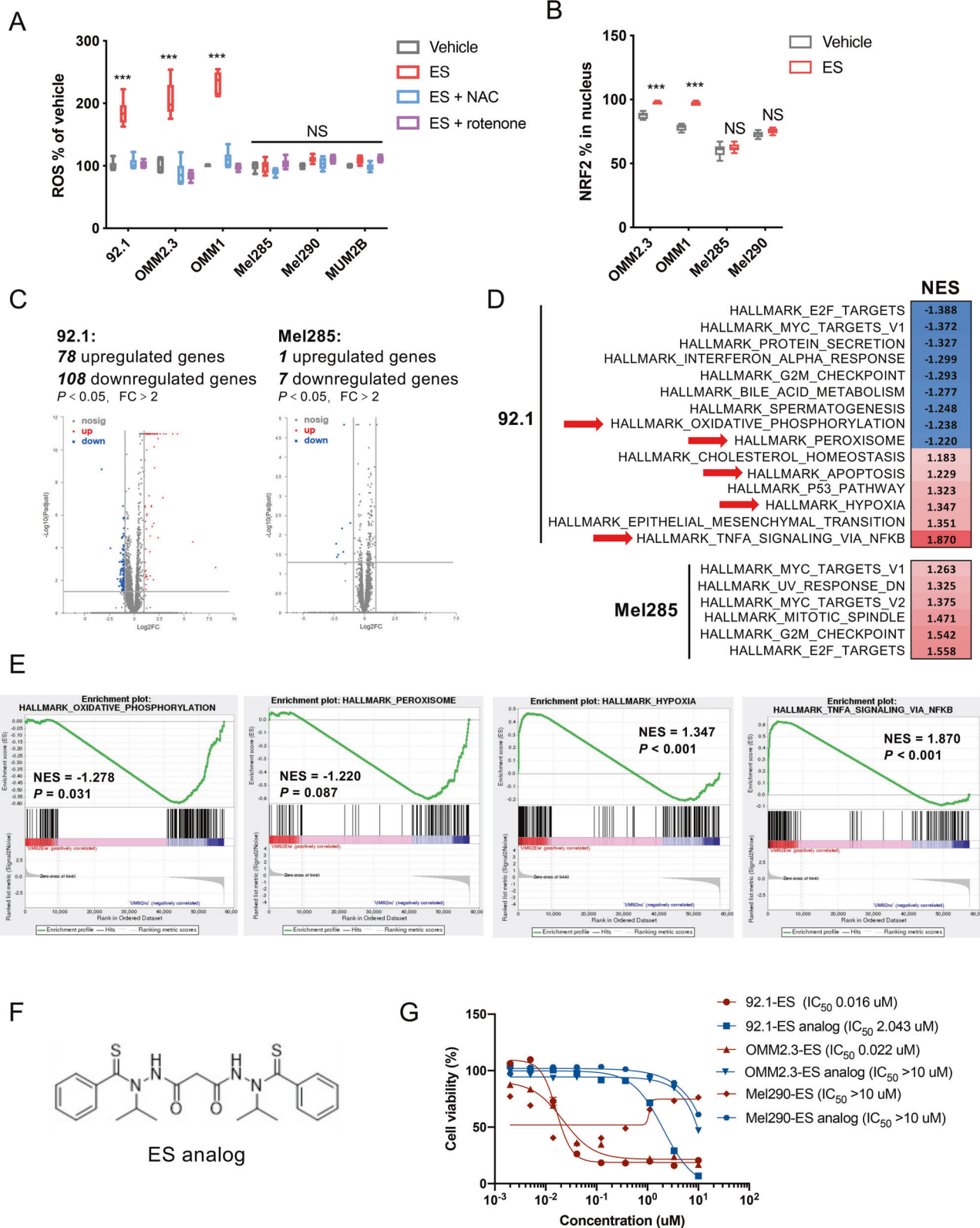
Next, we sought to elucidate whether elesclomol could trigger a distinct regulated cell death phenotype rather than apoptosis, necroptosis or ferroptosis, similar to other copper ionophores [30, 31]. Elesclomol was reported to cause a ferredoxin-dependent form of “cuproptosis” in NCI-H2030 cells [19] or apoptosis in K562 and KVP.5 cells [32]. Cell cycle analysis indicated that OMM1 and OMM2.3 cells were arrested in the G0/G1 phase after treatment with 100 nM elesclomol for 24 h ($p < 0.05$) but not Mel290 cells (Fig. 3A, Supplementary Fig. 3A). The proportion of OMM1 and OMM2.3 cells undergoing apoptosis was also sharply elevated after elesclomol treatment ($p < 0.001$), but this was not seen in Mel290 cells (Fig. 3B, Supplementary Fig. 3B). Western blot analysis data showed that elesclomol treatment led to a remarkable downregulation of c-Myc and cyclin D1 in OMM1 and OMM2.3 cells, which are required for cell cycle progression from G1 phase to S phase. In addition, cleaved caspase-3 was upregulated in OMM1 and OMM2.3 cells as the concentration of elesclomol increased (Fig. 3C, Supplementary Fig. 3C). Elesclomol altered the expression of the above proteins in a dose-dependent manner in *GNAQ/11*-mutant OMM1 and OMM2.3 cells but not in *GNAQ/11*-wild-type Mel290 cells. Elesclomol led to G0/G1 phase arrest and apoptosis in *GNAQ/11*-mutant UM cells, which was consistent with previous studies in different cell lines [33].

We were particularly interested in the long-term pharmacological efficacy of elesclomol in *GNAQ/11*-mutant cells, as it is well known that tumor cells are notoriously versatile and can adapt to environmental stress. Colony formation data showed that the growth of OMM1 and OMM2.3 cells was significantly suppressed by elesclomol at concentrations as low as 10 nM ($p < 0.001$), but the proliferation of Mel290 cells was not affected (Fig. 3D, Supplementary Fig. 3D).

Elesclomol impairs UM tumor growth in zebrafish and mouse models

To evaluate the in vivo efficacy of elesclomol on UM growth, we established an embryonic zebrafish xenograft model. This model offers live imaging possibilities to directly investigate UM cell migration and engagement under the action of different compounds [34]. After being stained with CM-Dil, 92.1 cells carried red fluorescence in their cell membrane and were injected into the yolk sac of zebrafish embryos 2 days post-fertilization (dpf) *Tg(kdr1:egfp)^{g116}*. After 6 days, the growth of the UM xenograft was observed in the yolk sac, and migration toward the eyes, main body vessel and tail was visible. The total tumor burden was then calculated (Supplementary Fig. 4A, B). The maximum tolerable dose was determined to be 10 μ M, with an 80% survival rate after a 6-day elesclomol treatment (Supplementary Fig. 4C); at this dose, the growth and migration of 92.1-CM-Dil cells were significantly reduced (Fig. 4A). The final tumor burden per embryo in the elesclomol group was significantly lower than that in the control group (3164 ± 402.8 , $n = 24$; 5714 ± 417.1 , $n = 24$; $p < 0.001$) (Fig. 4B).

To confirm the in vivo efficacy of elesclomol in a mammalian tumor model, a subcutaneous xenograft model was established in nude mice using 92.1 cells. Two doses, 25 mg/kg/day and 50 mg/kg/day, were administered to mice 5 days a week via tail vein injection, according to previous reports [35]. After ten administrations, the tumor-bearing UM mice treated with elesclomol showed significant tumor regression in both dose groups ($p < 0.05$; $p < 0.01$) (Fig. 4C, D, E, F), without a significant change in body weight (Supplementary Fig. 4D). To establish a correlation between efficacy and pharmacodynamic response, cells from the different mouse groups were isolated at the end of the efficacy study. The decrease in Ki67 and the increase in TUNEL in tumor tissue indicated an inhibition of cell proliferation and an increase in apoptosis in the tumors of the elesclomol treatment group (Fig. 4G, H).



Elesclomol induces YAP phosphorylation in *GNAQ/11*-mutant UM cells

Encouraged by the in vivo efficacy of elesclomol in the zebrafish as well as the mouse model, we analyzed the activity of MAPK/MEK/ERK, PI3K/Akt/mTOR, and Trio/Rho/Rac/YAP, all of which are

reported to be pathways downstream of *GNAQ/11* [36]. After 24 h of elesclomol treatment, the levels of ERK1/2 and AKT phosphorylation in four UM cell lines showed no sign of alteration, yet YAP (Ser127) phosphorylation was induced in a dose-dependent manner, which was more obvious in the *GNAQ/11*-mutant cell

Fig. 2 Elesclomol selectively elevates intracellular ROS in *GNAQ/11*-mutant UM cells. **A** The ROS levels were measured in six UM cell lines and normalized after 100 nM elesclomol treatment for 3 h. **B** Quantification of NRF2 intranuclear localization after elesclomol treatment at 100 nM for 3 h. **C** Volcano plot showing up- and downregulated genes in 92.1 and Mel285 cells after elesclomol treatment ($FC > 2$, $p < 0.05$). **D** Heatmap of selected GSEA hallmark pathways enriched in 92.1 cells treated with elesclomol versus the control (DMSO). The color scale ranks the indicated pathways based on their normalized enrichment score (NES). Blue and red indicate down- and upregulated pathways, respectively. **E** Enrichment plots of select GSEA pathways enriched in 92.1 cells treated with elesclomol versus control (DMSO), including oxidative phosphorylation, peroxisome, hypoxia and TNF α signaling via NF κ B. **F** The structure of the ES analog. **G** Representative dose–response curves of 92.1, OMM2.3, and Mel290 cells to elesclomol and its analog. Error bars represent the mean \pm SEM, $n = 3$ independent experiments for (A, B, C, G), * $p < 0.05$; ** $p < 0.01$; *** $p < 0.001$.

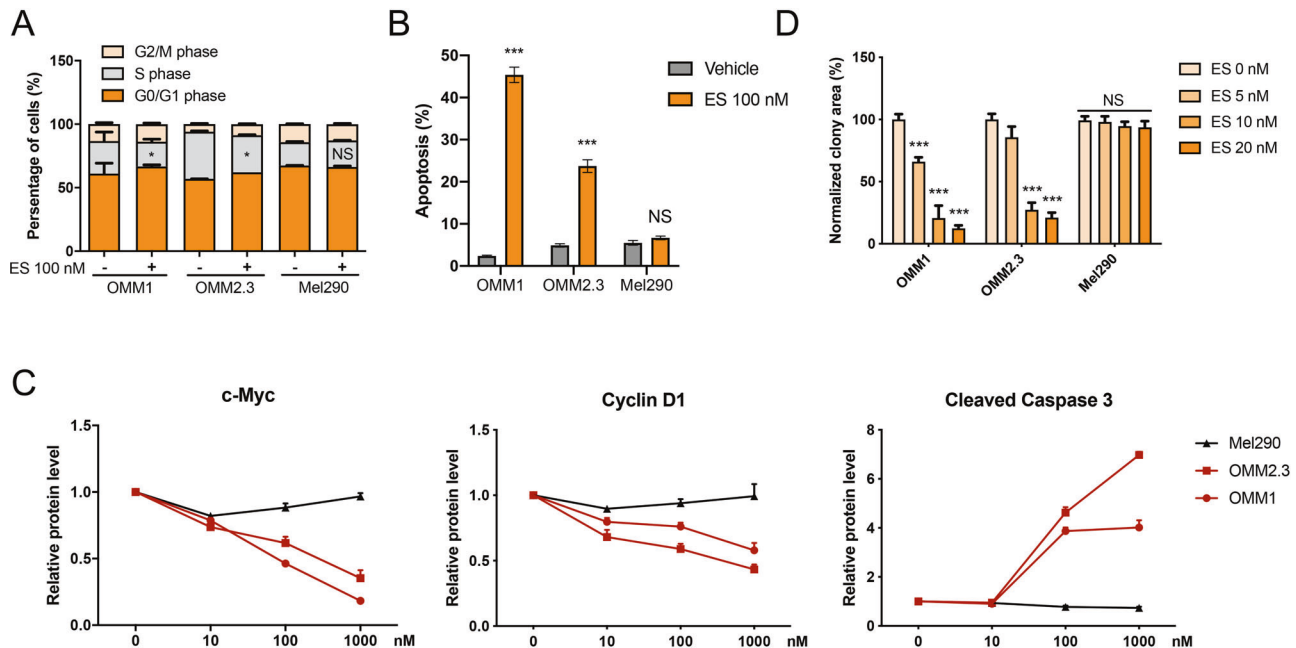


Fig. 3 Specific cellular events in elesclomol-treated *GNAQ/11*-mutant UM cells. Quantification of the cell cycle distribution (A) and apoptotic proportion (B) of UM cells treated with 100 nM elesclomol for 24 h. C Quantification of immunoblot analysis of c-Myc, cyclin D1, caspase-3 and cleaved caspase-3 proteins in UM cells treated for 24 h with selected concentrations of elesclomol. D Quantification of clonogenic growth of UM cells treated for 14 days with elesclomol at selected concentrations. Error bars represent the mean \pm SEM, $n = 3$ independent experiments for (A, B, C, D), * $p < 0.05$; ** $p < 0.01$; *** $p < 0.001$.

lines 92.1, OMM2.3, and OMM1 (Fig. 5A). The phosphorylation of YAP (Ser127) was also increased in a time-dependent manner in UM cells treated with 100 nM elesclomol (Fig. 5B). The p-YAP/YAP ratio increased significantly in *GNAQ/11*-mutant cells ($p < 0.001$) with prolonged exposure time but not in *GNAQ/11*-wild-type cells. However, the p-ERK/ERK ratio did not change in either cell type (Fig. 5C). Treatment with 100 nM elesclomol for 3 h blocked the nuclear translocation of YAP, as shown by its increased cytosolic fraction and decreased nuclear fraction, judged by YAP immunofluorescence detection (Fig. 5D) and western blot analysis (Fig. 5E). Elesclomol also suppressed the expression of endogenous YAP-regulated genes, including *CTGF* and *CYR61* ($p < 0.05$) (Fig. 5F). YAP nuclear localization was also repressed in the tumors of elesclomol-treated mice (Fig. 5G, H). Together, these findings suggest that elesclomol selectively induced YAP (Ser127) phosphorylation and YAP cytoplasmic sequestration in *GNAQ/11*-mutant UM cells both in vitro and in vivo.

The results prompted us to research the clinical link between the YAP phosphorylation level and *GNAQ/11* mutation status. In the tumor tissues of eight UM patients, the phosphorylation level of YAP was significantly lower in tumor samples with *GNAQ/11* mutation than in those without this mutation ($p < 0.01$) (Fig. 6A, B), indicating that YAP was abnormally activated in *GNAQ/11*-mutant UM and might serve as a therapeutic biomarker. When YAP was depleted by two siRNAs in OMM2.3 cells, the antiproliferative effect of elesclomol was attenuated (Supplementary Fig. 5A, Fig. 6C).

Further, overexpression of the *YAP^{S127A}-Flag* plasmid in *GNAQ*-mutant 92.1 cells significantly attenuated their sensitivity to elesclomol (Supplementary Fig. 5B, Fig. 6D). These results suggest that elesclomol might exert its pharmacological efficacy by inhibiting YAP activity.

To determine whether elesclomol regulates YAP phosphorylation via its upstream elements, the signaling status of the canonical Hippo pathway and noncanonical MAP4K family was examined. After exposure to elesclomol for 3 h, increased LATS1 phosphorylation at Thr1079 was detected in a dose-dependent manner, while the expression levels of members of the MAP4K family did not change (Fig. 6E, Supplementary Fig. 5C). Cotreatment with NAC (1 mM) or rotenone (2.5 μ M) inhibited the elesclomol-induced increase in p-LATS1 and p-YAP (Fig. 6F). These data support the notion that elevated ROS generation induced by elesclomol may directly contribute to activation of the LATS1-YAP cascade.

Elesclomol decreases the viability of MEKi-resistant UM cells

It was reported that copper influx enhances the *BRAF^{V600E}*-driven MAPK signaling pathway through a Cu-MEK1 interaction, which promotes the progression of SKCM in mice and humans [37]. We wondered if elesclomol could boost MEK inhibitor resistance in UM. Our screening compound library contains 18 MEK inhibitors, including trametinib, selumetinib, TAK-733, and binimetinib (Supplementary Table 2). Seven UM cell lines exhibited different

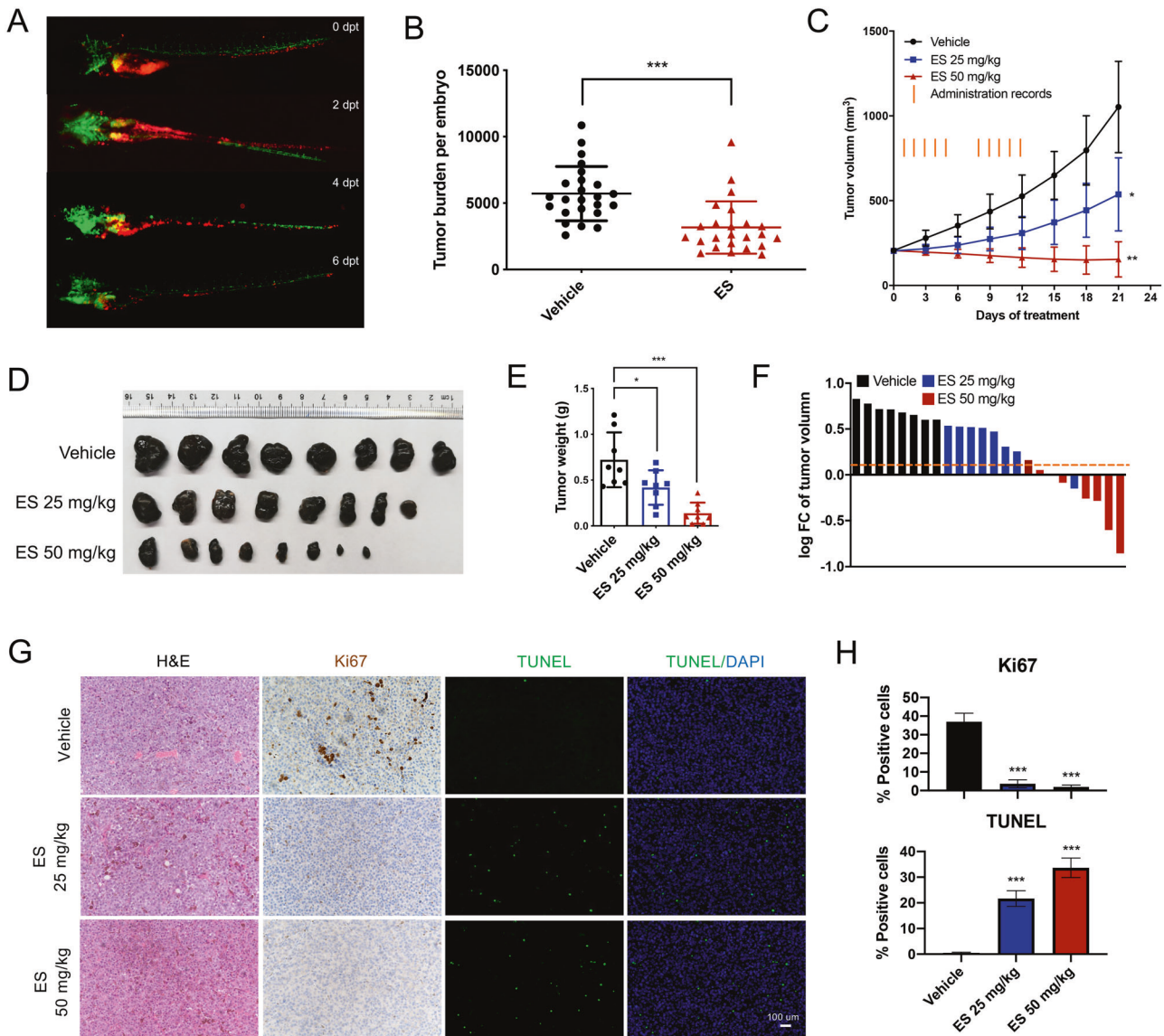


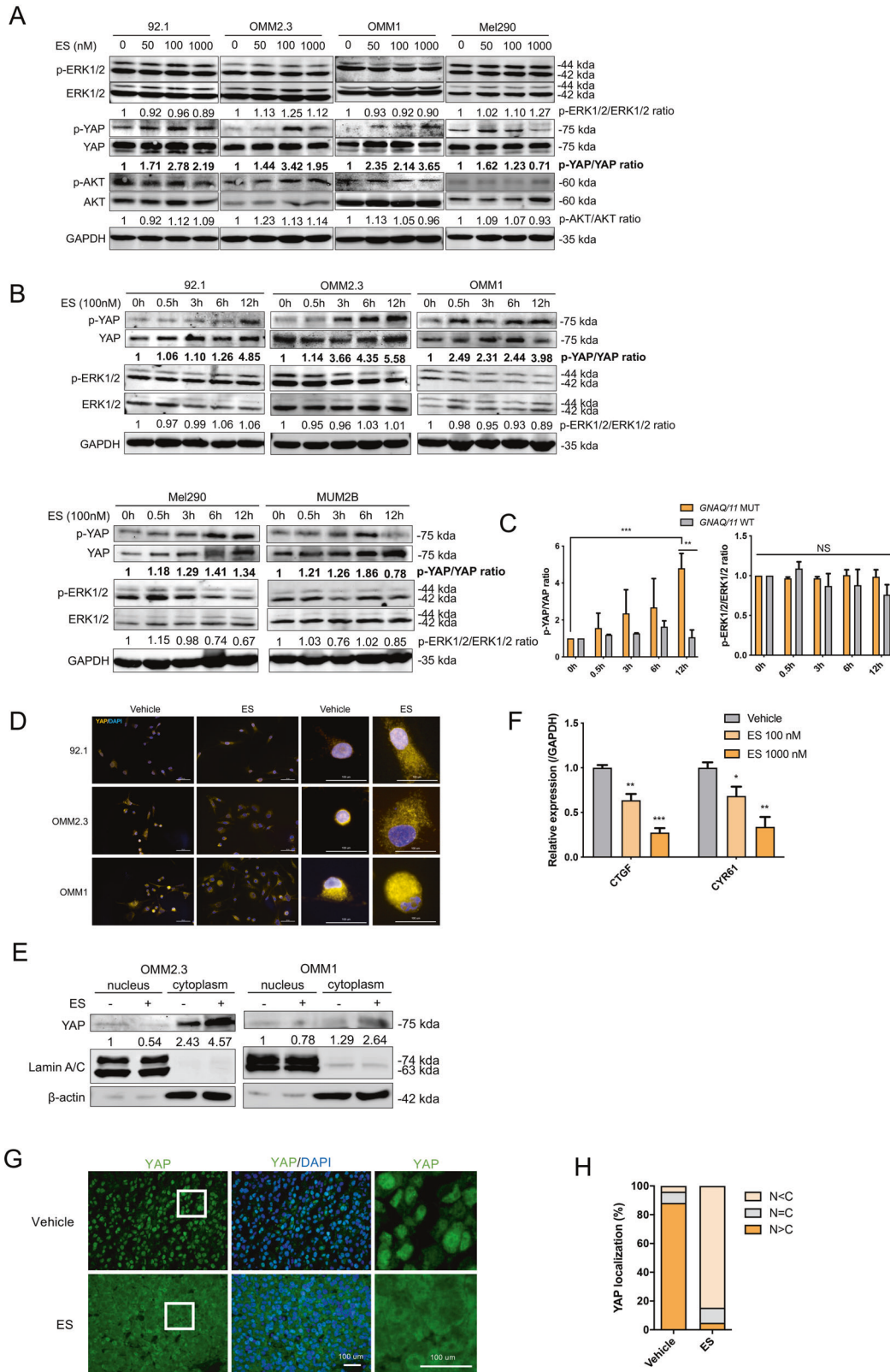
Fig. 4 Elesclomol impairs UM tumor growth in zebrafish and mouse models. **A** Representative fluorescence images of an embryo injected with 92.1-CM-Dil cells and treated with 10 μ M elesclomol. Images were captured at 0, 2, 4, and 6 days post-treatment (dpt). **B** Quantification of tumor burden per embryo was performed via automatic confocal analysis at 6 dpt with elesclomol or DMSO. **C** Average tumor volumes of 92.1 cell-derived xenografts after treatment with vehicle or elesclomol at 25 or 50 mg/kg for 10 days. The orange lines indicate the days of drug administration. **D** Tumors harvested after 21 days of treatment. **E** The mean weight of tumors in each group was compared. **F** Fold change in xenograft size, on the logarithmic (base 2) scale, after 10-day treatment with vehicle or elesclomol. The dotted line indicates a threshold of 10%-fold change. Representative images (**G**) and quantification (**H**) of H&E staining, Ki67 staining and TUNEL levels assessed by IHC and IF in the tumor tissues. Error bars represent the mean \pm SEM, $n = 24$ embryos in each group for (**B**), $n = 8$ mice in each group for (**C**), $*p < 0.05$; $**p < 0.01$; $***p < 0.001$. Scale bar, 100 μ m.

sensitivities to MEK inhibitors, among which OMM2.3 and OMM1 had the highest MEKi resistance (Supplementary Fig. 6A, B). We first tested whether elesclomol would abolish the efficacy of MEK inhibitors on MEKi-sensitive UM cells. The 92.1 cell line was chosen because it is relatively sensitive to binimetinib, with an IC_{50} of 78 nM (Supplementary Fig. 6C). In a fixed 1:1 ratio combination assay, the CI (combination index) [38] was 0.65 for 92.1 cells (Supplementary Fig. 6D). Apparently, elesclomol treatment did not attenuate but improved the efficacy of this MEKi in MEKi-sensitive UM cells.

Next, two strategies were used to evaluate the effect of the combination of elesclomol/binimetinib on MEKi-resistant cell lines. In a fixed ratio/combination assay (Fig. 7A), the CI was 0.30 and 0.25 for OMM2.3 and OMM1 cells, respectively, which indicated that elesclomol sensitized UM cells to MEK inhibition

(Supplementary Fig. 6E, F). Second, in a variable ratio/combination assay in OMM2.3 and OMM1 cells, the same effects were observed at elesclomol concentrations in the range of 1–100 nM when combined with binimetinib in the range of 74–2000 nM (Fig. 7B). Using a colony formation assay, we further confirmed that the killing effect of binimetinib on OMM2.3 and OMM1 cells could be enhanced by combination with elesclomol after prolonged treatment (Fig. 7C, D). Interestingly, the combination of binimetinib and elesclomol simultaneously inhibited ERK phosphorylation and increased YAP phosphorylation (Fig. 7E).

To further evaluate the effect of the elesclomol-MEKi combination in vivo, luciferase-labeled 92.1 cells were pretreated with 100 nM binimetinib or 10 nM elesclomol or their combination for 72 h before being orthotopically injected into the eyeballs of nude mice ($n = 4$ in each group). After 21 days of incubation, small



animal bioluminescence imaging analysis revealed weaker intensity of the tumor signal in the combination group than in the vehicle group and single-regimen groups ($p < 0.05$) (Fig. 7F, G). In the vehicle group, the eyeballs were filled with hyperpigmented tumors, and some of them showed tumor-related atrophy. There

were some residual tumors and tumor-related atrophy in the single-regimen-treated groups, whereas in the combination group, the eyeballs recovered to an almost crystal-clear status (Fig. 7H). After enucleation, the weight of the eyes (with the tumors) was found to be significantly reduced in the combination

Fig. 5 **Elesclomol selectively induces YAP phosphorylation in *GNAQ/11*-mutant UM cells.** **A** Immunoblot and quantitative analysis of p-ERK1/2 (phospho Thr202/Tyr204), total ERK1/2, p-YAP (phospho Ser127), total YAP, p-AKT (phospho Thr308) and total AKT in UM cells treated with elesclomol at select concentrations for 24 h. GAPDH was used as the loading control. **B** Immunoblot and quantitative analysis of p-ERK1/2, ERK1/2, p-YAP, and YAP in UM cells treated with elesclomol at 100 nM for selected exposure times. GAPDH was used as the loading control. **C** The p-YAP/YAP ratio and p-ERK1/2/ERK1/2 ratio in *GNAQ/11*-mutant and *GNAQ/11*-wild-type UM cell lines were calculated at selected exposure times. **D** Representative IF images of *GNAQ/11*-mutant UM cells showing the change in YAP localization after 100 nM elesclomol treatment for 6 h. **E** Cytosolic and nuclear fractions isolated from UM cells treated with elesclomol were analyzed via western blotting; β -actin and Lamin A/C were used as cytosolic and nuclear markers, respectively. **F** The expression of *CTGF* and *CYR61* after elesclomol treatment was determined via real-time qPCR. **G** IF analysis of YAP localization (**H**) and relative quantification (**H**) in the tumor tissues from the in vivo study. Error bars represent the mean \pm SEM, $n = 3$ independent experiments for (**A**, **B**, **D**, **E**, **F**), * $p < 0.05$; ** $p < 0.01$; *** $p < 0.001$. Scale bar, 100 μ m.

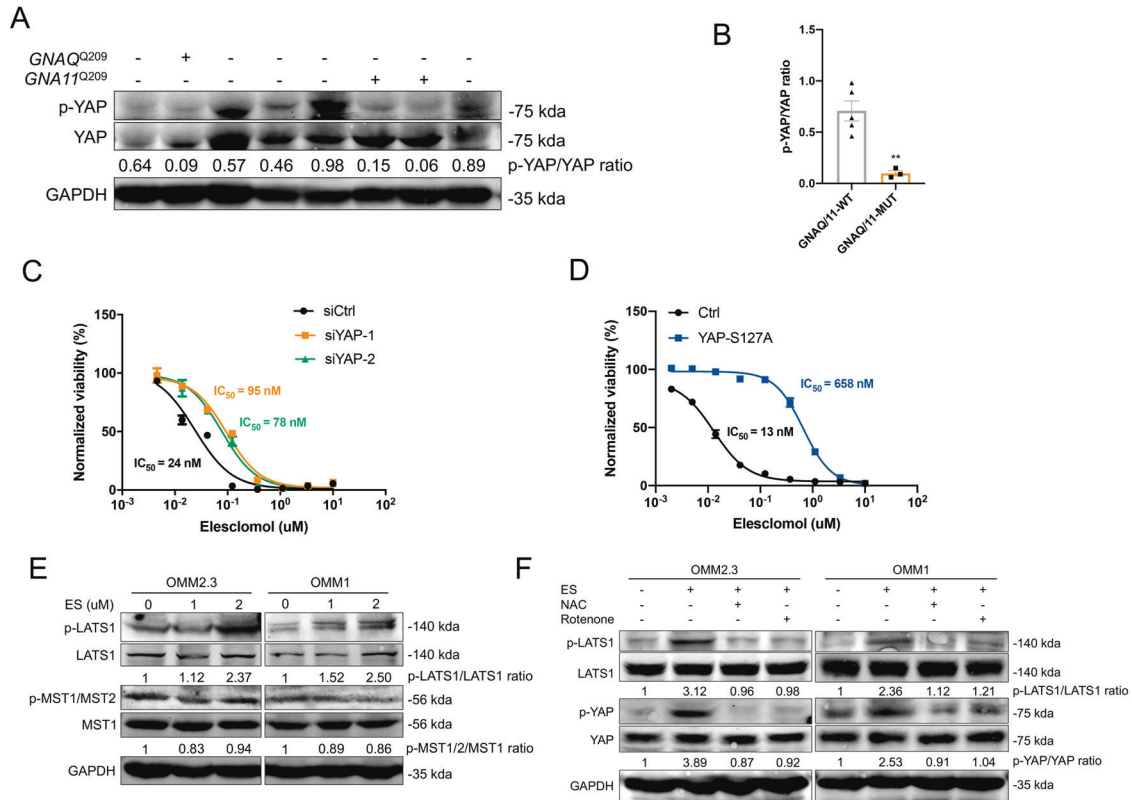


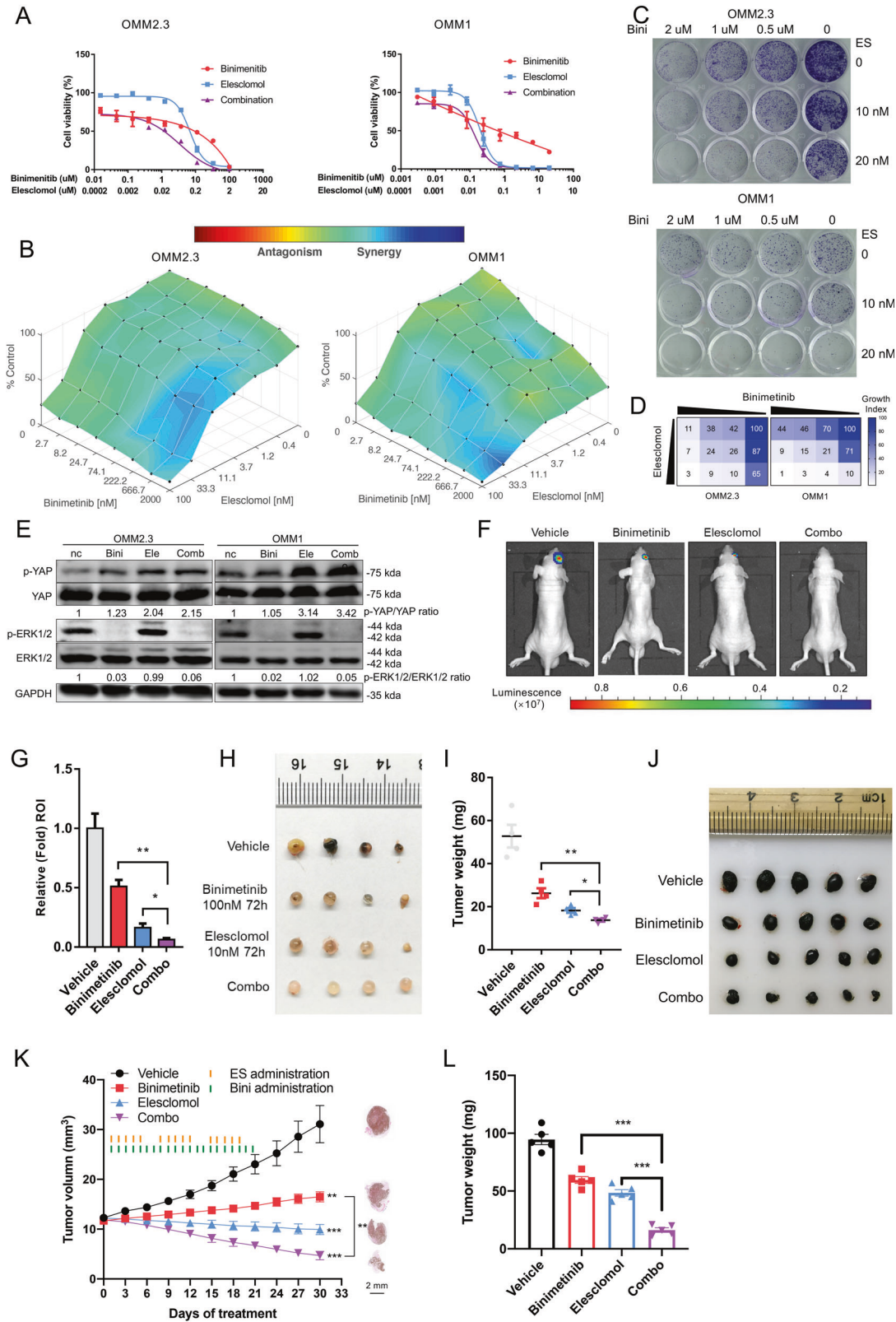
Fig. 6 **Elesclomol promotes YAP phosphorylation via ROS-induced Hippo signaling pathway activation.** **A** YAP protein and its phosphorylation level were detected via western blotting in tumor samples from eight UM patients. **B** The p-YAP/YAP ratio was calculated and compared between *GNAQ/11*-mutant and *GNAQ/11*-wild-type primary tumor tissues. **C** Representative dose-response curves for elesclomol-treated OMM2.3 cells transfected with siYAP or control siRNA. **D** Representative dose-response curves for elesclomol-treated 92.1 cells transfected with *YAP*^{S127A}-Flag or control plasmid. **E** Immunoblot analysis and quantification of p-LATS1 (phospho Thr1079), total LATS1, p-MST1/MST2 (phospho Thr180 + Thr183) and total MST1 in UM cells treated with elesclomol at select concentrations for 3 h. GAPDH was used as the loading control. **F** Immunoblot analysis and quantification of p-LATS1, LATS1, p-YAP, and YAP in UM cells treated with elesclomol with/without NAC or rotenone for 3 h. GAPDH was used as the loading control. Error bars represent the mean \pm SEM, $n = 3$ independent experiments for (**A**, **C**, **D**, **E**, **F**), * $p < 0.05$; ** $p < 0.01$; *** $p < 0.001$.

group ($p < 0.05$) (Fig. 7I). Notably, a patient-derived xenograft (PDX) model was established, and the results also demonstrated that combined treatment with binimetinib and elesclomol had a significantly greater inhibitory effect on tumor growth than the single-agent regimen, highlighting the potential of elesclomol to increase the efficacy of MEKis (Fig. 7J, K, L). Taken together, these data suggest that the combination of binimetinib and elesclomol blocked the YAP and MEK/ERK signaling pathways, which are constitutively activated in UM. The drug combination led to significant pharmacological efficacy against UM cells both in vitro and in vivo.

Elesclomol regulates *SNAI2* expression and cell migration

To elucidate the pharmacogenomic impact of elesclomol after alteration of YAP phosphorylation in MEKi-resistant *GNAQ/11*-

mutant UM cells, RNA-seq was conducted on OMM1 cells treated with 1 μ M elesclomol for 3 h. Using a threshold p value < 0.05 and $FC > 2$, 397 genes were found to be significantly up- or downregulated after elesclomol exposure. By taking the intersection with the Hippo signaling pathway, five differentially expressed genes stood out, among which *SNAI2* (*snail family transcriptional repressor 2*) ranked at the top of the list (Fig. 8A). *SNAI2* is a transcription factor in the Snail family with repressor activity [39] that dampens the expression of target genes, including *BRCA2* and *PUMA* [40, 41]. *SNAI2* is involved in initiating EMT by repressing *E-cadherin* expression and is associated with tumor invasion and metastasis and with poor prognosis in different malignancies [42–47]. The mRNA expression level of *SNAI2* was downregulated by 3-h treatment with 1 μ M elesclomol ($p < 0.001$) (Fig. 8B), and the protein expression level of *SNAI2* in



OMM2.3 and OMM1 cells was decreased after treatment with 25/50/100 nM elesclomol for 24 h (Fig. 8C). The correlation between YAP and *SNAI2* expression was demonstrated by an siRNA assay in OMM2.3 cells (Fig. 8D, E). Additionally, the *SNAI2* protein expression level was also repressed in the mouse tumor model after elesclomol treatment (Fig. 8F).

To investigate whether *SNAI2* influences the proliferation and migration of UM cells, siRNA was used to knockdown *SNAI2* expression (Supplementary Fig. 7A). CCK-8 assay results showed that decreasing *SNAI2* had little effect on cell proliferation (Supplementary Fig. 7B). However, wound healing assay and transwell assay results suggested that *SNAI2* had the capacity to

Fig. 7 Antiproliferative effect of elesclomol on MEKi-resistant UM cells. **A** Dose–response curves of the MEKi binimetinib, elesclomol, and their combination in the OMM2.3 and OMM1 cell lines. **B** OMM2.3 and OMM1 cells were treated for 72 h as indicated with elesclomol and binimetinib. FA values assessed at 56 different concentrations are shown utilizing Combenefit Software. **C** The colony formation ability of OMM2.3 and OMM1 cells was observed via crystal violet staining after 14 days of inoculation under elesclomol, binimetinib or combined treatment and quantified using ImageJ (**D**). **E** Immunoblot analysis and quantification of p-YAP (phospho Ser127), total YAP, p-ERK1/2 (phospho Thr202/Tyr204), and total ERK1/2 in UM cells treated with 1 μ M binimetinib, 100 nM elesclomol or the combined regimen for 3 h. GAPDH was used as the loading control. The 92.1 cell line was pretreated with binimetinib, elesclomol or the combined regimen for 72 h and injected orthotopically into the eyeballs of mice ($n = 4$ for each group). The tumor bioluminescence signals (**F**) and quantification (**G**) of 92.1 cells in orthotopic xenografts were obtained using an animal imaging system 21 days after injection. **H** Tumors were harvested 21 days after injection. **I** The weight of the eyes (with the tumors) was determined after 21 days of treatment. **J** Tumors harvested after 30 days of treatment. **K** Average tumor volumes of PDXs after treatment with vehicle, elesclomol, binimetinib or their combination for 21 days. The orange and green lines indicate the days of elesclomol and binimetinib administration, respectively. Representative images of H&E staining of tumor tissues from each group are shown on the right. **L** The mean weight of tumors in each group was compared. Error bars represent the mean \pm SEM, $n = 3$ independent experiments for (**A**, **B**, **C**, **E**), $n = 4$ mice in each group for (**F**), $n = 5$ mice in each group for (**J**), * $p < 0.05$; ** $p < 0.01$; *** $p < 0.001$.

promote cell migration: downregulating SNAI2 expression significantly suppressed the migration rate of OMM2.3 cells ($p < 0.001$) (Fig. 8G, H, I, J). Previous studies have shown that SNAI2 is under the control of YAP and reduces ROS production in leukemia stem cells [48, 49]. Collectively, these results demonstrate that elesclomol inhibits cell migration by promoting YAP phosphorylation and downregulating the expression of the SNAI2 gene.

DISCUSSION

The copper ionophore elesclomol provides a surprising new strategy for targeting *GNAQ/11*-mutant UM, as copper was previously reported to be required for oncogenic BRAF signaling and tumorigenesis in SKCM [37]. The distinct difference in sensitivity of *GNAQ/11*-mutant and *GNAQ/11*-wild-type UM cells to elesclomol led us to inquire if the basic ROS level was different in these two types of cells. By probing cells with H2DCFDA, we found no significant correlation between the intracellular ROS level and the *GNAQ/11* genetic status at baseline (Fig. 2, Supplementary Fig. 2). However, treatment with elesclomol generated a significant increase in ROS in *GNAQ/11*-mutant cells but not in *GNAQ/11*-wild-type cells. These data suggest that *GNAQ/11*-mutant UM cells may depend on a different metabolic pathway than wild-type cells and rely more on constitutive antioxidant activation to maintain their ROS level. Indeed, nuclear translocation of NRF2 was stimulated by elesclomol in *GNAQ/11*-mutant cells but not in *GNAQ/11*-wild-type cells. NRF2 helps to protect against mitochondrial damage caused by ROS by upregulating multiple antioxidant enzymes [50, 51]. GSEA of RNA-seq revealed that the expression of oxidative phosphorylation and peroxisome components was downregulated following elesclomol treatment, while hypoxia and apoptosis signaling were upregulated in *GNAQ*-mutant 92.1 cells.

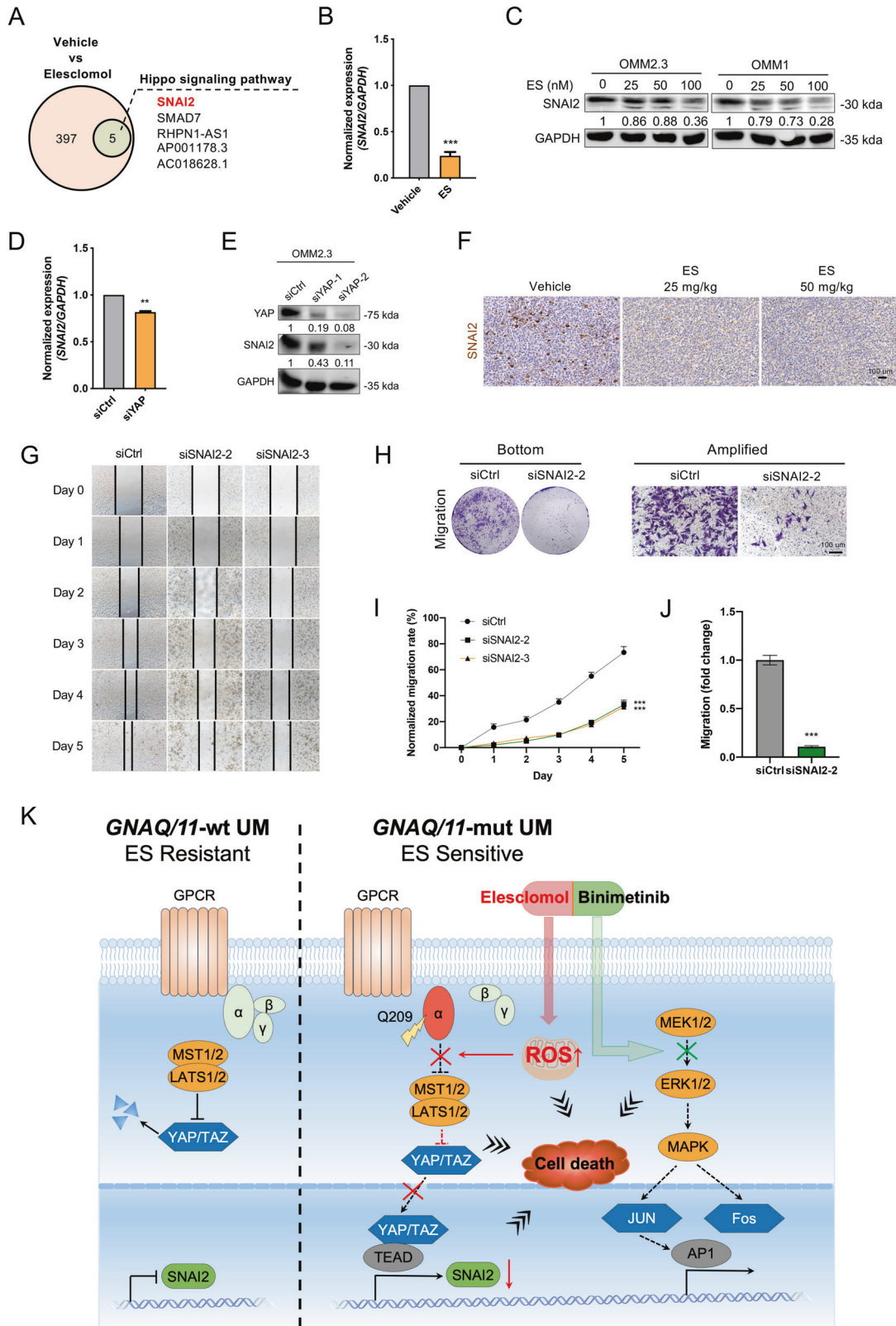
We speculate that cellular signal rewiring causes major differences in physiological adaptive behavior and chemosensitivity between *GNAQ/11*-wild-type and *GNAQ/11*-mutant UM. Interestingly, in contrast to previous findings that elesclomol boosts p-ERK and p-AKT activation in lung and breast cancer [52, 53], our results reveal that the phosphorylation level of YAP (Ser127) in *GNAQ/11*-mutant UM cells is significantly increased, rather than affecting the ERK and AKT cascades. This finding suggests that simultaneous targeting of the MEK and YAP signaling pathways may reduce the resistance of *GNAQ/11*-mutant cells to MEK inhibitors. Mutant *GNAQ/11* was found to be associated with dephosphorylation and nuclear localization of YAP, enhancing YAP-dependent transcription and thereby promoting UM tumorigenesis [9, 10, 54]. The correlation between the presence of *GNAQ/11* mutations and activated YAP was confirmed in eight UM samples. Notably, elesclomol significantly elevated the phosphorylation levels of LATS1 and YAP in a dose- and time-

dependent manner in *GNAQ/11*-mutant UM cell lines and retained YAP localization in the cytoplasm. Pretreatment of UM cells with NAC and rotenone significantly reduced elesclomol-induced upregulation of LATS1 and YAP phosphorylation. In kidney cancer, similar results showed that YAP/TAZ depletion diminished the growth of glycolysis-dependent tumors and increased mitochondrial respiration and ROS accumulation, leading to oxidative stress-induced cell death [55]. Thus, we propose that elesclomol exerts its specific killing of *GNAQ/11*-mutant UM cells by promoting the influx of copper into mitochondria and the induction of ROS, which triggers activation of the LATS1-YAP axis (Fig. 8K). The connection between ROS elevation and LATS1 activation remains to be explored in *GNAQ/11*-mutant UM cells.

The use of elesclomol has been tried but failed to achieve favorable outcomes in several clinical studies conducted among refractory solid tumors, including SKCM, ovarian cancer, pancreatic cancer, and colorectal cancer [21–24]. We speculate that several factors contributed to this failure. First, the method of administration needs to be discussed. Although elesclomol is a safe agent, because of the strong side effects of paclitaxel [22], the combined infusion of elesclomol and paclitaxel limited the frequency of administration [23, 24]. Based on the mechanism by which elesclomol exerts its pharmacological effect through binding with Cu [18, 19], we speculate that prechelation of elesclomol with copper may improve its efficacy.

Second, patient selection is crucial for elesclomol therapy, as we revealed here that UM cells with different genetic backgrounds showed significantly different responses. In fact, combined data from two randomized phase II and phase III trials showed that elesclomol prolonged PFS time in patients with metastatic SKCM with low lactate dehydrogenase (LDH) levels [23, 24]. However, the criterion of low LDH should not be the sole factor determining the sensitivity of a tumor to elesclomol. Physiological LDH levels are likely regulated by many factors beyond hypoxia [20] and consistently change with tumor progression [23]. Proposing cancers with certain oncogenic drivers and copper metabolic addiction would be more practical. In *KRAS*-mutated colorectal cancer, upregulated expression of the copper-exporter ATP7A is essential to protect cancer cells from excess copper toxicity [56]. Interestingly, the cellular function of *GNAQ/11* is largely equivalent to the function of *Ras*. High expression of ATP7A is also significantly correlated with reduced survival in breast cancer patients [57].

Third, a tumor's genetic background and its specific vulnerability to copper metabolism should be taken into consideration when choosing a drug combination. Here, we demonstrate that elesclomol can sensitize *GNAQ/11*-mutant UM cells to MEK inhibition in vitro and in vivo. In current clinical trials, MEK inhibitors are the most commonly used targeted therapeutics. However, UM responds poorly to MEK inhibitors [14]. In MEKi-resistant UM cells, the oxidative stress sensor SNAI2 [48] was



downregulated in response to elesclomol treatment. Although SNAI2 does not affect the proliferation of UM cells, it can significantly enhance their migration ability, and tumor metastasis is the main cause of death in UM patients. Our study provides a potential synthetic drug option for UM patients who show

resistance or acquired resistance to MEKis. Mechanistically, elesclomol and binimetinib synergistically inhibit two separate signaling pathways to prevent the progression of UM.

Unlike SKCM, the mortality of UM is still high due to the lack of effective targeted therapies and immune agents. Therefore, more

Fig. 8 Elesclomol regulates *SNAI2* expression and cell migration through YAP. **A** Wayne diagram showing differentially expressed genes, including those in the Hippo pathway, after elesclomol treatment. *SNAI2* is at the top among the five genes in the intersection. Downregulation of *SNAI2* expression after elesclomol treatment was detected via real-time qPCR (**B**) and western blotting (**C**). The expression of *SNAI2* after YAP knockdown via siRNA was determined by real-time qPCR (**D**) and western blotting (**E**). **F** IHC analysis of *SNAI2* in tumor tissues from the in vivo study. The migration activity of OMM2.3 cells transfected with *SNAI2* siRNA or control siRNA was determined by wound healing assays (**G**) and transwell assays (**H**). The migration rate in the wound healing assay (**I**) and transwell assay (**J**) was quantified with ImageJ. **K** A schematic representation of the mechanism by which elesclomol selectively targets *GNAQ/11*-mutant UM. Mutant *GNAQ/11* cells respond to elesclomol by producing abnormally high levels of cellular ROS, which promotes YAP phosphorylation and nuclear sequestration through activation of LATS1 kinase. This subsequently downregulates *SNAI2* expression by inducing YAP inactivation and suppresses UM cell migration. By targeting two independent signaling pathways, the combination of elesclomol/binimetinib can synergistically inhibit the growth of binimetinib-resistant UM cells. Error bars represent the mean \pm SEM, $n = 2$ independent experiments for (**A**), $n = 3$ independent experiments for (**B**, **C**, **D**, **E**, **G**, **H**), * $p < 0.05$; ** $p < 0.01$; *** $p < 0.001$. Scale bar, 100 μm .

effective strategies and novel therapeutics are desperately needed for this disease. This study reveals the fundamental mechanistic understanding that copper homeostasis is a *GNAQ/11*-specific vulnerability in UM. We envision that copper ionophores, such as elesclomol, may provide a new therapeutic path for selectively antagonizing malignant *GNAQ/11* mutants when these compounds have improved drug-like properties with appropriate administration and patient selection protocols are identified.

MATERIALS AND METHODS

Cell lines

The UM cell lines 92.1, OMM2.3, OMM1, Mel285, Mel290 and XMP46 were generously provided by Prof. MJJ (Leiden University Medical Center, Leiden, The Netherlands) [58–63]. OMM2.3, OMM1, Mel285, Mel290, MUM2B and XMP46 cells were cultured in Roswell Park Memorial Institute (RPMI) 1640 medium supplemented with 10% fetal bovine serum (FBS) in the presence of penicillin/streptomycin. The 92.1 cell line was cultured in RPMI 1640 medium supplemented with 10% FBS. The primary UM patient-derived cell line was established from UM tumors upon mechanical dissection of tissue and cultured in RPMI 1640 medium supplemented with 10 mM N-2-hydroxyethylpiperazine-N-2-ethane sulfonic acid (HEPES) and 10% FBS in the presence of penicillin/streptomycin. Cells were maintained in a humidified incubator at 37 °C with 5% CO₂.

Mouse orthotopic and subcutaneous tumor models

Five-week-old male BALB/c nude mice were obtained from Shanghai Jie Si Jie Laboratory Animals Co. Ltd.

For cell line-derived subcutaneous models, 92.1 cells were inoculated subcutaneously into the right flank of mice at a concentration of 5×10^5 cells/ μl in 100 μl RPMI 1640 medium with 100 μl Matrigel (BD). For PDX models, fresh tumor samples from a UM patient with the *GNAQ*^{Q209} mutation were collected for subcutaneous implantation into the right flank of mice under the associated informed consent. Tumors were measured every 3 days with a caliper, and tumor volume was calculated using the following formula: tumor volume = width \times width \times length $\times 0.52$.

For orthotopic models, each animal was deeply anesthetized with chloral hydrate, and the cornea was anesthetized with Benoxil. Methocel eye drops were applied to avoid dryness of the eyes. Injections were performed using a surgical microscope. Then, 2 μl PBS containing 2×10^4 pretreated and luciferase-labeled 92.1 cells were injected into the subchoroidal area of each eye through the limbus using a Hamilton syringe. After the injection, the eyes were treated with antibiotic eye ointment. After 21 days, bioluminescence was determined using a small in vivo animal imaging system. All mice were euthanized after tumor formation analysis, and tumor samples were collected.

Elesclomol efficacy studies

Elesclomol was purchased from Selleck Chemicals (Shanghai, China). The formulation of elesclomol explored in this study was a single reagent without Cu. The elesclomol solution used in the mouse models contained 40% PEG 300 and 5% Tween 80. Mice were divided into three groups: the vehicle control group in which the mice were treated with saline with the same schedule as the treated animals; the elesclomol 25 mg/kg group; and the elesclomol 50 mg/kg group in which mice were treated with elesclomol (25 mg/kg or 50 mg/kg, i.v. injection for 5 days/week for 2 weeks) ($n = 8$ for each group).

Elesclomol and binimetinib efficacy studies

Binimetinib was purchased from Selleck Chemicals (Shanghai, China). For the orthotopic model, 2×10^4 luciferase-labeled 92.1 cells were pretreated with four different drug treatment protocols and injected into the subchoroidal area of the eye. Vehicle control group ($n = 4$): cells were pretreated with DMSO with the same schedule as the treated groups; binimetinib group ($n = 4$): cells were pretreated with 100 nM binimetinib for 72 h; elesclomol group ($n = 4$): cells were pretreated with 10 nM elesclomol for 72 h; combination group ($n = 4$): cells were pretreated with 100 nM binimetinib and 10 nM elesclomol for 72 h. The tumors were harvested after 21 days. The tumor bioluminescence signals in the orthotopic xenografts were visualized using an animal imaging system. For the PDX model, mice were randomly divided into four groups ($n = 5$ in each group). Vehicle control group: the mice were treated with saline with the same schedule as the treated animals; binimetinib group: mice were treated with binimetinib (3 mg/kg, oral gavage, once a day for 21 days); elesclomol group: mice were treated with elesclomol (25 mg/kg, i.v. injection for 5 days/week for 21 days); combination group: mice were treated with binimetinib and elesclomol simultaneously.

Xenograft models in zebrafish

92.1 cells were stained with CM-Dil (Invitrogen) for 4 min at 37 °C, incubated for 15 min on ice in the dark, washed with PBS 2 times and taken up in 2% polyvinylpyrrolidone-40 (PVP-40). Approximately 300 CM-Dil-labeled cells were injected into the yolk sac of anesthetized 2-dpf *Tg* (*kdr:egfp*)^{la116} zebrafish embryos using glass capillary needles (Holliston) with an approximate opening equal to the dimension of one cell, and treatment started at 24 h post-injection (hpi). The concentration of elesclomol was determined based on a safety test in which 2-dpf embryos were immersed in egg water containing elesclomol, and a survival rate after 6 days > 80% was considered tolerable. The egg water with drug was replaced every 2 days ($n = 24$ for each group). Stereo images were taken with a Nikon SMZ25 stereomicroscope. Confocal images were acquired using a confocal microscope (Nikon Microsystems). Image processing was performed with ImageJ. Each individual red fluorescent cluster inside the embryo was detected. The total tumor burden per embryo was estimated by multiplying the mean area of all tumor foci by the total number of red objects.

Drug screening

Using an automated platform, we tested three annotated libraries with a total of 3541 compounds in seven UM cell lines (92.1, OMM2.3, OMM1, Mel285, Mel290, MUM2B and XMP46). Cells were seeded in a 384-well format and treated with individual compounds at a concentration of 2 μM before evaluation of cell viability after 72 h (two doubling times) using a CellTiter-Glo Luminescent assay (Promega). The initial screening was replicated twice. The log₂ fold change (compound/DMSO) in cell viability for each compound was calculated, and a value below -2 was defined as UM sensitive (Supplementary Table 2). Further evaluation of compounds that allowed more than 50% inhibition of cell viability was performed in a nine-point threefold dilution series of each compound before evaluation of cell viability after 72 h using a CCK-8 assay (Dojindo). Three replications were performed. Dose–response curves were fitted, and the IC₅₀ value of the candidate compounds was calculated using GraphPad 7.0 software. The preference of the compounds for *GNAQ/11*-mutant or *GNAQ/11*-wild-type UM cells was determined using the index log₁₀ value (relative IC₅₀ ratio).

Synthesis of the elesclomol analog ELE-003 without copper binding capacity

Synthesis of ELE-003: 1-Boc-2-isopropylhydrazine and benzoyl chloride generated Compound 1, which was dissolved in dichloromethane, and then, trifluoroacetic acid was added to remove the BOC protective group. After sulfur oxygen exchange with Lawson reagent, Compound 3 was obtained. Two equivalents of Compound 3 and one equivalent of malonic acid were reacted with EDCI to afford the target compound ELE-003. ELE-003 was dissolved in ethanol solution, and then, 2 equivalents of copper(II) chloride dihydrate was added. The mixture was stirred at room temperature for 1 h and then detected via LCMS. No MS signal of the desired chelated molecule was detected (data not shown). Thus, it was concluded that ELE-003 did not chelate copper ions.

Western blot analysis

Approximately 6×10^5 cells were seeded into 6-cm plates and cultured in the presence or absence of drugs as indicated. Phospho-lysis buffer (50 mM Tris pH 7.5, 1% Tween-20, 200 mM NaCl, 0.2% NP-40) supplemented with phosphatase inhibitors and protease inhibitors (Promega) was used for cell lysis, and the protein concentration was determined using a BCA protein assay (Pierce) according to the instructions. SDS-polyacrylamide gel electrophoresis was performed using 8 to 12% Bis-Tris gels, and proteins were transferred to polyvinylidene difluoride (PVDF) membranes (Millipore) via semidry transfer in Trans-Blot transfer medium (Bio-Rad). Membranes were blocked in 5% nonfat milk and incubated overnight at 4 °C with primary antibodies. Primary antibodies targeting the following proteins were used: c-Myc (Abcam, ab32072), cyclin D1 (Abcam, ab134175), caspase-3 (Proteintech, 19677-1-AP), cleaved caspase-3 (Cell Signaling, 9661), p-ERK1/2 (phospho Thr202/Tyr204, Cell Signaling, 4370), ERK1/2 (Cell Signaling, 9107), p-YAP (phospho Ser127, Abcam, ab76252), YAP (Proteintech, 66900-1-Ig), p-AKT (phospho Thr308, Cell Signaling, 13038), AKT (Cell Signaling, 4691), p-LATS1 (phospho Thr1079, Cell Signaling, 8654), LATS1 (Proteintech, 17049-1-AP), p-MST1/MST2 (phospho Thr180 + Thr183, Abcam, ab76323), MST1 (Proteintech, 22245-1-AP), Flag (Cell Signaling, #14793), SNAI2 (Proteintech, 12129-1-AP), GNAQ (Proteintech, 13927-1-AP), and GAPDH (Abcam, ab8245). After repeated washes with TBST, the blots were incubated with the appropriate secondary antibody and imaged using a CLx Detection System (Odyssey). Grayscale analysis was performed using ImageJ software. Each experiment was performed in triplicate.

siRNA and YAP^{S127A}-flag transfection

GNAQ siRNA oligonucleotides (siGNAQ-1: 5'-UUGUGCAUGAGCCUUAUUG-3', siGNAQ-2: 5'-UCGUCUAUCAUAGCAUCC-3'), YAP siRNA oligonucleotides (siYAP-1: 5'-CUGCCACCAAGCUAGAUAA-3', siYAP-2: 5'-GAUACCUGAUGAU GUACCU-3'), SNAI2 siRNA oligonucleotides (siSNAI2-1: 5'-CGGACCCACACA UUACCUU-3', siSNAI2-2: 5'-CCGAAUGUCUCUCCUGC-3', siSNAI2-3: 5'-ACU ACAGUCCAAGCUUUA-3') and control siRNA (siNC: 5'-ATCCACTACCGTTGT TATAGGTG-3') were designed based on published synthetic siRNA sequences (Biotend Co, Ltd, Shanghai, China). The plasmid YAP^{S127A}-Flag (#17790, p2xFLAGhYAP1-S127A) was purchased from Addgene. Cells were transfected with the plasmid and siRNAs using Lipofectamine 2000 (Invitrogen) according to the manufacturer's instructions.

Colony formation, cell cycle arrest, and apoptosis assays

For colony formation assessment, cells were seeded into six-well plates (2×10^3 cells per well) and allowed to adhere overnight in regular growth medium. Cells were then cultured in the absence or presence of drug as indicated in complete medium for 10–14 days. Growth medium with or without drug was replaced every 3 days. The remaining cells were fixed with 4% paraformaldehyde (PFA), stained with 10% crystal violet, and photographed using a digital scanner. Relative growth was quantified using ImageJ. All experiments were performed at least three times. Representative experiments are shown.

For cell cycle arrest analysis, approximately 1×10^6 cells were cultured in the presence or absence of drugs as indicated for 24 h, harvested in chilled 70% ethanol, and stored at 4 °C overnight. Then, the cells were labeled with propidium iodide (40 µg/ml, Thermo Fisher Scientific) for 30 min at 37 °C. The cell cycle distribution was determined using a FACSCalibur system (BD, USA) and analyzed with ModFit LT software.

For apoptosis assays, approximately 1×10^6 cells were cultured in the presence or absence of drugs as indicated. After 24 h, apoptosis and cell death were determined using an Annexin V-APC apoptosis detection kit according to the manufacturer's instructions (Affymetrix eBioscience). Data

were acquired using a FACSCalibur system (BD, USA). Each independent experiment was performed three times.

Immunohistochemistry

Tissues were perfused with 4% PFA, stored in fixative overnight, and embedded in paraffin. For further staining with hematoxylin and eosin (H&E) and antibodies, 5 µm sections were cut. After deparaffinization and antigen retrieval, the tissues were permeabilized with 0.3% Triton X-100, incubated with 0.3% H₂O₂ solution to quench endogenous peroxidase activity, and blocked with 5% goat serum in PBS. Antibodies were optimized using a predetermined staining protocol: Ki67 (Cell Signaling, 9449) and SNAI2 (Proteintech, 12129-1-AP). The slides were developed using diaminobenzidine (DAB) (Maxim, China) and mounted. Next, the slides were observed and photographed using a Nikon Eclipse Ni Microscope (Nikon, Japan).

Immunofluorescence

Cells were fixed with 4% PFA for 10 min at room temperature, permeabilized with 0.3% Triton X-100 in PBS for 15 min and blocked in 5% BSA in PBS for 30 min at room temperature. The cells were then incubated with primary antibodies against NRF2 (Proteintech, 16396-1-AP) and YAP (Proteintech, 66900-1-Ig), and Alexa Fluor-conjugated secondary antibodies were used. Cell nuclei were stained with DAPI reagent (Abcam, ab104139). TUNEL assays were performed according to the manufacturer's instructions (Millipore). Sample analysis and image acquisition were performed using a Nikon Eclipse 80i Microscope (Nikon, Japan).

Measurement of intracellular ROS

ROS production in the cell lines was determined using the fluorescent dye chloromethyl-2',7'-dichlorofluorescein diacetate (H2DCFDA, Thermo Fisher Scientific). Adherent cells were plated at 5000 cells/well in a 96-well clear-bottom black plate overnight before treatment. Cells were treated with 100 nM elesclomol or DMSO for 3 h at 37 °C, washed with PBS and incubated with 10 µM H2DCFDA at 37 °C for 30 min in PBS while protected from light. After loading of the fluorescent dye, the cells were washed twice with PBS and resuspended in 100 µl PBS. To measure ROS levels, fluorescence was captured with a Nikon Eclipse 80i Microscope (Nikon, Japan) and measured using a SpectraMax iD3 (Molecular Devices) microplate reader. Three biological replicates were performed for each group.

RNA-based next-generation sequencing (RNA-seq)

92.1 and Mel285 cells (1×10^7) were treated with 25 nM elesclomol or DMSO for 24 h. OMM1 cells (1×10^7) were treated with 1 µM elesclomol or DMSO for 3 h. Total RNA was extracted using TRIzol reagent (Takara, Japan). The cDNA was amplified and labeled with a Quick Amp Labeling Kit (Agilent Technologies, USA) and hybridized onto an Agilent oligo microarray. Statistical analysis and data normalization were conducted with Genespring GX software (Agilent Technology). For differential gene expression, $p < 0.05$ and an absolute fold change > 2 were used to identify significantly altered genes. Pathway analysis was performed using Gene Set Enrichment Analysis (v3.0). Three biological replicates were prepared for each group.

RNA extraction and real-time PCR analysis

Total RNA was extracted using TRIzol reagent (Takara), and cDNA was synthesized using a PrimeScript RT reagent kit (Takara) according to the manufacturer's instructions. Real-time PCR was performed using PowerUp SYBR Green Master Mix (Thermo Fisher Scientific) with specific primers (Supplementary Table 3) for GAPDH (housekeeping gene), YAP, CTGF, CYR61, MAP4K1, MAP4K2, MAP4K3, MAP4K4, MAP4K5 and SNAI2.

Nuclear and cytoplasmic extraction

We used a nuclear-cytosol extraction kit to separate the cytoplasmic and nuclear proteins (Thermo Fisher Scientific) according to the manufacturer's instructions. Fractions were analyzed via SDS-PAGE and western blotting with specific antibodies against YAP (Proteintech, 66900-1-Ig), Lamin A/C (Abcam, ab108595), and β-actin (Abcam ab8226).

Growth kinetic assay in vitro

The growth kinetics of cells were determined using a Cell Counting Kit 8 (CCK-8, Dojindo) assay. Cells were plated in triplicate at a density of 2000

cells/well in 96-well plates, and the absorbance value was measured at a wavelength of 450 nm using a BioTek Epoch 2 microplate reader (BioTek, USA) every 24 h after seeding.

Wound healing assay

Cells were plated in 6-well plates at a density of 1×10^6 cells per well. After the cells attached to the bottom of the plate, wounds were generated using sterilized pipette tips, and the medium was substituted with medium containing 1% FBS. Images of the plates from the same point of view were observed and captured every 24 h.

Transwell migration assay

The migratory ability of cells was evaluated using a transwell system (Corning) according to the manufacturer's instructions. Each chamber with 8- μ m pores contained 10000 cells and was placed in a 24-well plate containing medium with 1% FBS. The lower compartment contained 20% FBS. After 48 h of incubation at 37 °C, the cells that had migrated into the lower chamber were stained with crystal violet dye and then washed with 100 μ l of 33% acetic acid. The absorbance of the wash liquid was determined with a BioTek Epoch 2 microplate reader (BioTek, USA) at 630 nm.

Quantitative analysis of drug combinations

Drug synergism was analyzed using CalcuSyn software, which is based on the median-effect principle and the combination index-isobologram theorem (Chou-Talalay) [38]. CalcuSyn software generates combination index (CI) values, where $CI < 0.75$ indicates synergism, $CI = 0.75-1.25$ indicates additive effects, and $CI > 1.25$ indicates antagonism. Following the instructions of the software, drug combinations at nonconstant ratios were used to calculate the combination index in our study.

Quantification and statistical analysis

Statistical analyses were performed using GraphPad 7.0 software. Data are presented as the mean \pm standard error of the mean (S.E.M.). The number of technical replicates or independent biological repeats is indicated in the figure legends. Unpaired two-tailed Student's *t* test and two-way ANOVA were utilized as appropriate. Survival plots were generated based on Kaplan–Meier curves. Correlations were analyzed using Pearson's correlation coefficient (*r*) and the *p* value. No samples, mice or data points were excluded from the analyses. For all analyses, the results were considered statistically significant at **p* < 0.05; ***p* < 0.01; ****p* < 0.001; *****p* < 0.0001.

DATA AVAILABILITY

All sequencing data are available through the Gene Expression Omnibus (GEO) via accession code PRJNA733836.

REFERENCES

- Singh AD, Topham A. Incidence of uveal melanoma in the United States: 1973-97. *Ophthalmology*. 2003;110:956-61.
- Shields CL, Shields JA. Ocular melanoma: relatively rare but requiring respect. *Clin Dermatol*. 2009;27:122-33.
- Khoja L, Atenafu EG, Suci S, Leyvraz S, Sato T, Marshall E, et al. Meta-analysis in metastatic uveal melanoma to determine progression free and overall survival benchmarks: an international rare cancers initiative (IRCI) ocular melanoma study. *Ann Oncol*. 2019;30:1370-80.
- Van Raamsdonk CD, Bezrookove V, Green G, Bauer J, Gaugler L, O'Brien JM, et al. Frequent somatic mutations of GNAQ in uveal melanoma and blue naevi. *Nature*. 2009;457:599-602.
- Van Raamsdonk CD, Griewank KG, Crosby MB, Garrido MC, Vemula S, Wiesner T, et al. Mutations in GNA11 in uveal melanoma. *N Engl J Med*. 2010;363:2191-9.
- Smit KN, Jager MJ, de Klein A, Kili E. Uveal melanoma: towards a molecular understanding. *Prog Retin Eye Res*. 2020;75:100800.
- Kleuss C, Raw AS, Lee E, Sprang SR, Gilman AG. Mechanism of GTP hydrolysis by G-protein alpha subunits. *Proc Natl Acad Sci USA*. 1994;91:9828-31.
- Populo H, Soares P, Rocha AS, Silva P, Lopes JM. Evaluation of the mTOR pathway in ocular (uvea and conjunctiva) melanoma. *Melanoma Res*. 2010;20:107-17.
- Feng X, Degese MS, Iglesias-Bartolome R, Vaque JP, Molinolo AA, Rodrigues M, et al. Hippo-independent activation of YAP by the GNAQ uveal melanoma oncogene through a trio-regulated rho GTPase signaling circuitry. *Cancer Cell*. 2014;25:831-45.
- Yu FX, Luo J, Mo JS, Liu G, Kim YC, Meng Z, et al. Mutant Gq/11 promote uveal melanoma tumorigenesis by activating YAP. *Cancer Cell*. 2014;25:822-30.
- Campbell AP, Smrcka AV. Targeting G protein-coupled receptor signalling by blocking G proteins. *Nat Rev Drug Discov*. 2018;17:789-803.
- Schrage R, Schmitz AL, Gaffal E, Annala S, Kehraus S, Wenzel D, et al. The experimental power of FR900359 to study Gq-regulated biological processes. *Nat Commun*. 2015;6:10156.
- Onken MD, Makepeace CM, Kaltenbronn KM, Kanai SM, Todd TD, Wang S, et al. Targeting nucleotide exchange to inhibit constitutively active G protein alpha subunits in cancer cells. *Sci Signal*. 2018;11:ea06852.
- Steeb T, Wessely A, Ruzicka T, Heppt MV, Berking C. How to MEK the best of uveal melanoma: a systematic review on the efficacy and safety of MEK inhibitors in metastatic or unresectable uveal melanoma. *Eur J Cancer*. 2018;103:41-51.
- Long GV, Stroyakovskiy D, Gogas H, Levchenko E, de Braud F, Larkin J, et al. Combined BRAF and MEK inhibition versus BRAF inhibition alone in melanoma. *N Engl J Med*. 2014;371:1877-88.
- Ambrosini G, Musi E, Ho AL, de Stanchina E, Schwartz GK. Inhibition of mutant GNAQ signaling in uveal melanoma induces AMPK-dependent autophagic cell death. *Mol Cancer Ther*. 2013;12:768-76.
- Shoushtari AN, Kudchadkar RR, Panageas K, Murthy RK, Jung M, Shah R, et al. A randomized phase 2 study of trametinib with or without GSK2141795 in patients with advanced uveal melanoma. *J Clin Oncol*. 2016;34:9511.
- Nagai M, Vo NH, Shin Ogawa L, Chimmanamada D, Inoue T, Chu J, et al. The oncology drug elesclomol selectively transports copper to the mitochondria to induce oxidative stress in cancer cells. *Free Radic Biol Med*. 2012;52:2142-50.
- Tsvetkov P, Detappe A, Cai K, Keys HR, Brune Z, Ying W, et al. Mitochondrial metabolism promotes adaptation to proteotoxic stress. *Nat Chem Biol*. 2019;15:681-9.
- Hedley D, Shamas-Din A, Chow S, Sanfelice D, Schuh AC, Brandwein JM, et al. A phase I study of elesclomol sodium in patients with acute myeloid leukemia. *Leuk Lymphoma*. 2016;57:2437-40.
- Monk BJ, Kauderer JT, Moxley KM, Bonebrake AJ, Dewdney SB, Secord AA, et al. A phase II evaluation of elesclomol sodium and weekly paclitaxel in the treatment of recurrent or persistent platinum-resistant ovarian, fallopian tube or primary peritoneal cancer: An NRG oncology/gynecologic oncology group study. *Gynecol Oncol*. 2018;151:422-7.
- Berkenblit A, Eder JP Jr., Ryan DP, Seiden MV, Tatsuta N, Sherman ML, et al. Phase I clinical trial of STA-4783 in combination with paclitaxel in patients with refractory solid tumors. *Clin Cancer Res*. 2007;13:584-90.
- O'Day SJ, Eggermont AM, Chiarion-Sileni V, Kefford R, Grob JJ, Mortier L, et al. Final results of phase III SYMMETRY study: randomized, double-blind trial of elesclomol plus paclitaxel versus paclitaxel alone as treatment for chemotherapy-naïve patients with advanced melanoma. *J Clin Oncol*. 2013;31:1211-8.
- O'Day S, Gonzalez R, Lawson D, Weber R, Hutchins L, Anderson C, et al. Phase II, randomized, controlled, double-blinded trial of weekly elesclomol plus paclitaxel versus paclitaxel alone for stage IV metastatic melanoma. *J Clin Oncol*. 2009;27:5452-8.
- Parry D, Guzi T, Shanahan F, Davis N, Prabhavalkar D, Wiswell D, et al. Dinaciclib (SCH 727965), a novel and potent cyclin-dependent kinase inhibitor. *Mol Cancer Ther*. 2010;9:2344-53.
- Carlson BA, Dubay MM, Sausville EA, Brizuela L, Worland PJ. Flavopiridol induces G1 arrest with inhibition of cyclin-dependent kinase (CDK) 2 and CDK4 in human breast carcinoma cells. *Cancer Res*. 1996;56:2973-8.
- Gunst JD, Kjaer K, Olesen R, Rasmussen TA, Ostergaard L, Denton PW, et al. Fimepinostat, a novel dual inhibitor of HDAC and PI3K, effectively reverses HIV-1 latency ex vivo without T cell activation. *J Virus Erad*. 2019;5:133-7.
- Harrington BS, Ozaki MK, Caminear MW, Hernandez LF, Jordan E, Kalinowski NJ, et al. drugs targeting tumor-initiating cells prolong survival in a post-surgery, post-chemotherapy ovarian cancer relapse model. *Cancers*. 2020;12:1645.
- Harris IS, DeNicola GM. The Complex Interplay between Antioxidants and ROS in Cancer. *Trends Cell Biol*. 2020;30:440-51.
- Shimada K, Reznik E, Stokes ME, Krishnamoorthy L, Bos PH, Song Y, et al. Copper-binding small molecule induces oxidative stress and cell-cycle arrest in glioblastoma-patient-derived cells. *Cell Chem Biol*. 2018;25:585-94.e7.
- Tardito S, Bassanetti I, Bignardi C, Elvirri L, Tegoni M, Mucchino C, et al. Copper binding agents acting as copper ionophores lead to caspase inhibition and paraptotic cell death in human cancer cells. *J Am Chem Soc*. 2011;133:6235-42.
- Hasinoff BB, Wu X, Yadav AA, Patel D, Zhang H, Wang DS, et al. Cellular mechanisms of the cytotoxicity of the anticancer drug elesclomol and its complex with Cu(II). *Biochem Pharmacol*. 2015;93:266-76.
- Kirshner JR, He S, Balasubramanyam V, Kepros J, Yang CY, Zhang M, et al. Elesclomol induces cancer cell apoptosis through oxidative stress. *Mol Cancer Ther*. 2008;7:2319-27.

34. van der Ent W, Burrello C, Teunisse AF, Ksander BR, van der Velden PA, Jager MJ, et al. Modeling of human uveal melanoma in zebrafish xenograft embryos. *Investig Ophthalmol Vis Sci*. 2014;55:6612–22.
35. Kluzza J, Corazao-Rozas P, Touil Y, Jendoubi M, Maire C, Guerreschi P, et al. Inactivation of the HIF-1 α /PDK3 signaling axis drives melanoma toward mitochondrial oxidative metabolism and potentiates the therapeutic activity of pro-oxidants. *Cancer Res*. 2012;72:5035–47.
36. Li Y, Shi J, Yang J, Ge S, Zhang J, Jia R, et al. Uveal melanoma: progress in molecular biology and therapeutics. *Ther Adv Med Oncol*. 2020;12:1758835 920965852.
37. Brady DC, Crowe MS, Turksi ML, Hobbs GA, Yao X, Chaikuad A, et al. Copper is required for oncogenic BRAF signalling and tumorigenesis. *Nature*. 2014;509:492–6.
38. Chou TC. Drug combination studies and their synergy quantification using the Chou-Talalay method. *Cancer Res*. 2010;70:440–6.
39. Nieto MA, Sargent MG, Wilkinson DG, Cooke J. Control of cell behavior during vertebrate development by Slug, a zinc finger gene. *Science*. 1994;264:835–9.
40. Wu WS, Heinrichs S, Xu D, Garrison SP, Zambetti GP, Adams JM, et al. Slug antagonizes p53-mediated apoptosis of hematopoietic progenitors by repressing puma. *Cell*. 2005;123:641–53.
41. Tripathi MK, Misra S, Khedkar SV, Hamilton N, Irvin-Wilson C, Sharan C, et al. Regulation of BRCA2 gene expression by the SLUG repressor protein in human breast cells. *J Biol Chem*. 2005;280:17163–71.
42. Bolos V, Peinado H, Perez-Moreno MA, Fraga MF, Esteller M, Cano A. The transcription factor Slug represses E-cadherin expression and induces epithelial to mesenchymal transitions: a comparison with Snail and E47 repressors. *J Cell Sci*. 2003;116:499–511.
43. Barrallo-Gimeno A, Nieto MA. The Snail genes as inducers of cell movement and survival: implications in development and cancer. *Development*. 2005;132:3151–61.
44. Hajra KM, Chen DY, Fearon ER. The SLUG zinc-finger protein represses E-cadherin in breast cancer. *Cancer Res*. 2002;62:1613–8.
45. Fan H, Wang X, Li W, Shen M, Wei Y, Zheng H, et al. ASB13 inhibits breast cancer metastasis through promoting SNAIL2 degradation and relieving its transcriptional repression of YAP. *Genes Dev*. 2020;34:1359–72.
46. Li W, Shen M, Jiang YZ, Zhang R, Zheng H, Wei Y, et al. Deubiquitinase USP20 promotes breast cancer metastasis by stabilizing SNAIL2. *Genes Dev*. 2020;34:1310–5.
47. Asnaghi L, Gezgin G, Tripathy A, Handa JT, Merbs SL, van der Velden PA, et al. EMT-associated factors promote invasive properties of uveal melanoma cells. *Mol Vis*. 2015;21:919–29.
48. Zhang Z, Li L, Wu C, Yin G, Zhu P, Zhou Y, et al. Inhibition of Slug effectively targets leukemia stem cells via the Slc13a3/ROS signaling pathway. *Leukemia*. 2020;34:380–90.
49. Wang W, Hind T, Lam BWS, Herr DR. Sphingosine 1-phosphate signaling induces SNAIL2 expression to promote cell invasion in breast cancer cells. *FASEB J*. 2019;33:7180–91.
50. Ma Q. Role of nrf2 in oxidative stress and toxicity. *Annu Rev Pharmacol Toxicol*. 2013;53:401–26.
51. Hayes JD, Dinkova-Kostova AT. The Nrf2 regulatory network provides an interface between redox and intermediary metabolism. *Trends Biochem Sci*. 2014;39:199–218.
52. Albayrak G, Korkmaz FD, Tozcu D, Dogan, Turacli I. The outcomes of an impaired powerhouse in KRAS mutant lung adenocarcinoma cells by Elesclomol. *J Cell Biochem*. 2019;120:10564–71.
53. Qu Y, Wang J, Sim MS, Liu B, Giuliano A, Barsoum J, et al. Elesclomol, counteracted by Akt survival signaling, enhances the apoptotic effect of chemotherapy drugs in breast cancer cells. *Breast Cancer Res Treat*. 2010;121:311–21.
54. Brouwer NJ, Konstantinou EK, Gragoudas ES, Marinkovic M, Luyten GPM, Kim IK, et al. Targeting the YAP/TAZ pathway in uveal and conjunctival melanoma with verteporfin. *Investig Ophthalmol Vis Sci*. 2021;62:3.
55. White SM, Avantaggiati ML, Nemazany I, Di Poto C, Yang Y, Pende M, et al. YAP/TAZ inhibition induces metabolic and signaling rewiring resulting in targetable vulnerabilities in NF2-deficient tumor cells. *Dev Cell*. 2019;49:425–43.e9.
56. Aubert L, Nandagopal N, Steinhart Z, Lavoie G, Nourredine S, Berman J, et al. Copper bioavailability is a KRAS-specific vulnerability in colorectal cancer. *Nat Commun*. 2020;11:3701.
57. Shanbhag V, Jasmer-McDonald K, Zhu S, Martin AL, Gudekar N, Khan A, et al. ATP7A delivers copper to the lysyl oxidase family of enzymes and promotes tumorigenesis and metastasis. *Proc Natl Acad Sci USA*. 2019;116:6836–41.
58. De Waard-Siebinga I, Blom DJ, Griffioen M, Schrier PI, Hoogendoorn E, Beverstock G, et al. Establishment and characterization of an uveal-melanoma cell line. *Int J Cancer*. 1995;62:155–61.
59. Chen PW, Murray TG, Uno T, Salgaller ML, Reddy R, Ksander BR. Expression of MAGE genes in ocular melanoma during progression from primary to metastatic disease. *Clin Exp Metastasis*. 1997;15:509–18.
60. Luyten GP, Naus NC, Mooy CM, Hagemeyer A, Kan-Mitchell J, Van Drunen E, et al. Establishment and characterization of primary and metastatic uveal melanoma cell lines. *Int J Cancer*. 1996;66:380–7.
61. Ksander BR, Rubsamen PE, Olsen KR, Cousins SW, Streilein JW. Studies of tumor-infiltrating lymphocytes from a human choroidal melanoma. *Investig Ophthalmol Vis Sci*. 1991;32:3198–208.
62. Amirouchene-Angelozzi N, Nemati F, Gentien D, Nicolas A, Dumont A, Carita G, et al. Establishment of novel cell lines recapitulating the genetic landscape of uveal melanoma and preclinical validation of mTOR as a therapeutic target. *Mol Oncol*. 2014;8:1508–20.
63. Seftor EA, Meltzer PS, Kirschmann DA, Pe'er J, Maniotis AJ, Trent JM, et al. Molecular determinants of human uveal melanoma invasion and metastasis. *Clin Exp Metastasis*. 2002;19:233–46.

ACKNOWLEDGEMENTS

This research was supported by the National Natural Science Foundation of China (grant 82073889), the Science and Technology Commission of Shanghai (20DZ2270800), the Shanghai Municipal Science and Technology Major Project (19JC1410200), the National Facility for Translational Medicine (Shanghai) (TMSZ-2020-206), the Innovative Research Team of High-level Local Universities in Shanghai (SHSMU-ZDCX20210900), and startup funding of State Key Laboratory of Medical Genomics to JZ. We thank Drs. David E. Fisher and Xu Wu (Massachusetts General Hospital), Yantao Chen, and Yunqi Li (Shanghai Jiao Tong University) for review of this work and discussions on various topics relating to this project.

AUTHOR CONTRIBUTIONS

JZ, YL, and JY designed and performed the experiments; JY, SX, and SG were responsible for the animal model; YL, JY, QZ, XX, and RJ analyzed the data; WS designed the ES analog ELE-003; YL, JZ, MJJ, and XF drafted the paper. All authors read and approved the final paper.

COMPETING INTERESTS

The authors declare no competing interests.

ETHICS APPROVAL AND CONSENT TO PARTICIPATE

For the patient-derived cell line and the tissue used for the PDX model, written informed consent was obtained from all involved patients. The process was approved by the ethics committee of Shanghai Ninth People's Hospital (reference number: 20202356). For animal experiments, all procedures followed were in accordance with the Declaration of Helsinki. All animal research was conducted in accordance with the ARVO Statement for the Use of Animals in Ophthalmic and Vision Research, all procedures were reviewed and approved by Shanghai Ninth People's Hospital Central Lab IACUC (Permit Number: SYXK (Shanghai) 2016-0016), and all experiments conformed to the relevant regulatory standards. The experimental design followed the Guide for the Care and Use of Laboratory Animals of AAALAC international.

ADDITIONAL INFORMATION

Supplementary information The online version contains supplementary material available at <https://doi.org/10.1038/s41388-022-02364-0>.

Correspondence and requests for materials should be addressed to Renbing Jia, Jianming Zhang or Xianqun Fan.

Reprints and permission information is available at <http://www.nature.com/reprints>

Publisher's note Springer Nature remains neutral with regard to jurisdictional claims in published maps and institutional affiliations.